The Astrophysical Journal, 779:44 (25pp), 2013 December 10 doi:10.1088/0004-637X/779/1/44


# PROBABILITY DISTRIBUTION FUNCTIONS OF $^{12}$CO($J = 1 \rightarrow 0$) BRIGHTNESS AND INTEGRATED INTENSITY IN M51: THE PAWS VIEW

Annie Hughes[1], Sharon E. Meidt[1], Eva Schinnerer[1], Dario Colombo[1], Jerôme Pety[2,3], Adam K. Leroy[4], Clare L. Dobbs[5], Santiago García-Burillo[6], Todd A. Thompson[7,8], Gaëlle Dumas[2], Karl F. Schuster[2], and Carsten Kramer[9]

[1] Max-Planck-Institut für Astronomie, Königstuhl 17, D-69117 Heidelberg, Germany
[2] Institut de Radioastronomie Millimétrique, 300 Rue de la Piscine, F-38406 Saint Martin d'Hères, France
[3] Observatoire de Paris, 61 Avenue de l'Observatoire, F-75014 Paris, France
[4] National Radio Astronomy Observatory, 520 Edgemont Road, Charlottesville, VA 22903, USA
[5] School of Physics and Astronomy, University of Exeter, Stocker Road, Exeter EX4 4QL, UK
[6] Observatorio Astronómico Nacional, Observatorio de Madrid, Alfonso XII, 3, E-28014 Madrid, Spain
[7] Department of Astronomy, The Ohio State University, 140 West 18th Avenue, Columbus, OH 43210, USA
[8] Center for Cosmology and AstroParticle Physics, The Ohio State University, 191 West Woodruff Avenue, Columbus, OH 43210, USA
[9] Instituto Radioastronomía Milimétrica, Avenida Divina Pastora 7, Nucleo Central, E-18012 Granada, Spain
*Received 2012 August 20; accepted 2013 February 11; published 2013 November 25*

## ABSTRACT

We analyze the distribution of CO brightness temperature and integrated intensity in M51 at ∼40 pc resolution using new $^{12}$CO($J = 1 \rightarrow 0$) data from the Plateau de Bure Arcsecond Whirlpool Survey (PAWS). We present probability distribution functions (PDFs) of the CO emission within the PAWS field of view, which covers the inner ∼11 × 7 kpc of M51. We find clear variations in the shape of CO PDFs both within different M51 environments, defined according to dynamical criteria, and among M51 and two nearby low-mass galaxies, M33 and the Large Magellanic Cloud (LMC). Globally, the PDFs for the inner disk of M51 can be represented by narrow lognormal functions that cover ∼1–2 orders of magnitude in CO brightness and integrated intensity. The PDFs for M33 and the LMC are narrower and peak at lower CO intensities, consistent with their lower gas surface densities. However, the CO PDFs for different dynamical environments within the PAWS field depart significantly from the shape of the global distribution. The PDFs for the interarm region are approximately lognormal, but in the spiral arms and central region of M51, they exhibit diverse shapes with a significant excess of bright CO emission. The observed environmental dependence on the shape of the CO PDFs is qualitatively consistent with changes that would be expected if molecular gas in the spiral arms is characterized by a larger range of average densities, gas temperatures, and velocity fluctuations, although further work is required to disentangle the relative importance of large-scale dynamical effects versus star formation feedback in regulating these properties. We show that the shape of the CO PDFs for different M51 environments is only weakly related to global properties of the CO emission, e.g., the total CO luminosity, but is strongly correlated with properties of the local giant molecular cloud (GMC) and young stellar cluster populations, including the shape of their mass distributions. For galaxies with strong spiral structure such as M51, our results indicate that galactic-scale dynamical processes play a significant role in the formation and evolution of GMCs and stellar clusters.

*Key words:* galaxies: individual (M51, M33, Large Magellanic Cloud) – galaxies: ISM – ISM: molecules – ISM: structure

## 1. INTRODUCTION

Although the interstellar medium (ISM) represents a minor fraction of the baryonic matter in galaxies, it plays an important role in their evolution, providing the raw fuel for star formation (SF), receiving and then redistributing heavy elements created in stellar interiors and mediating the exchange of matter and energy between galaxies and the intergalactic medium (IGM). Conditions in the ISM are influenced by multiple physical processes occurring across a range of temporal and spatial scales, including accretion of primordial IGM material, protostellar jets and outflows, spiral shocks, supernovae, and thermal instability in the diffuse atomic gas. As a consequence of this diverse physics, interstellar gas occurs in multiple phases, with temperatures, densities, and spatial structures that span five orders of magnitude or more.

Due to its complex hierarchical structure, a quantitative analysis of ISM properties and dynamics is challenging. The intensity of emission from ISM structures can be characterized in terms of a fractal index (e.g., Elmegreen & Falgarone 1996) or power spectrum (e.g., Block et al. 2010), while properties of the velocity field can be summarized using a power spectrum or by the use of structure functions (e.g., Brunt et al. 2003). The density (and column density) structure of the ISM is most commonly represented using a probability distribution function (PDF; e.g., Kainulainen et al. 2009). Density PDFs of the ISM are supposed to follow a lognormal (LN) distribution. One of the most widespread explanations for an LN distribution is that the expected density PDF resulting from a turbulent velocity field is LN (e.g., Padoan et al. 1997). Simulations of supersonically turbulent isothermal gas find that the width of the density PDF increases with the rms Mach number (e.g., Padoan & Nordlund 2002) and that the precise form of the relationship depends on the relative importance of compressible and solenoidal modes in the turbulence forcing (Federrath et al. 2008, 2010). Comparison with observations of the Taurus and IC5146 molecular clouds indicates that turbulent driving in the ISM must contain a significant compressive component or that the width of the density PDF depends on additional physics that is not included in the simulations (Price et al. 2011). However, these models

apply only on the scale of individual molecular clouds, where the assumption of isothermality is reasonable, not to whole galaxies. The properties of ISM turbulence should depend on the energy injection scale and the height of the galactic disk, both of which will become relevant for galactic-scale systems. As noted by previous authors (e.g., Wada & Norman 2007), the PDFs of galaxies and individual molecular clouds cannot be directly compared since a galaxy's total molecular gas content cannot be characterized by a single temperature or a spatially uniform, time-independent Mach number.

In spite of these considerations, LN PDFs are still apparent in galaxy-scale simulations (e.g., Wada & Norman 2007; Dobbs et al. 2008; Tasker & Bryan 2006). The LN shape of the density PDFs emerges quickly in the simulations (i.e., within a local dynamical time) and is surprisingly robust to a diverse range of additional input physics (e.g., magnetic fields and energy feedback from stellar winds and supernovae; Wada & Norman 2001; Dobbs et al. 2011). The characteristic density of high- and low-mass models is roughly invariant ($\langle n \rangle \sim 1$ cm$^{-3}$) for disks with initial mass densities spanning an order of magnitude (e.g., Wada & Norman 2007). The proposed explanation for why LN density PDFs appear to be generic is that galactic disks are globally stable, with a hierarchical density structure that results from the action of a large number of stochastic, independent and nonlinear processes. In this case, the density PDF should evolve toward an LN shape by the central limit theorem (e.g., Vazquez-Semadeni 1994). Notably, the only simulation in Dobbs et al. (2011) that shows a strong departure from an LN PDF is the one with very low SF efficiency and hence a low level of thermal and kinetic energy feedback into the ISM. In this case, the model galaxy disk does not achieve an equilibrium state, since most of the interstellar gas becomes quickly confined to dense, gravitationally bound clumps (C. Dobbs, 2012 private communication).

More recently, LN density PDFs have gained more significance, as they have been used as the basis for explaining the Kennicutt–Schmidt (KS) relation (Schmidt 1959; Kennicutt 1998). The KS relation relates the surface density of gas to the SF rate surface density according to $\Sigma_{\rm SFR} = A\Sigma_{\rm gas}^{n}$. On global scales (i.e., averaged over entire star-forming disks), Kennicutt (1998) obtained $A = (2.5 \pm 0.7) \times 10^{-4}$ and $n = 1.4 \pm 0.15$ for a composite sample of ∼100 normal and starburst galaxies. The KS relation can also be written using the molecular gas surface density only, in which case $n$ is nearly linear (e.g., Wong & Blitz 2002; Bigiel et al. 2008, 2011). That an LN density PDF for the interstellar gas might naturally yield the KS relation was first suggested by Elmegreen (2002) and later developed in more detail by Kravtsov (2003), Krumholz & McKee (2005), and Wada & Norman (2007). The PDF is used to find the fraction of gas above a given density threshold, which is assumed to collapse and form stars. Summing up the mass of gas at each density divided by the free fall time provides the SF rate. This approach also forms the basis of the universal SF law recently proposed by Krumholz et al. (2012).

In spite of the potential importance of the ISM's hierarchical structure to the interpretation of extragalactic SF laws, observational evidence to support a universal LN density PDF for galactic disks remains scarce. Gaustad & van Buren (1993) used the *Infrared Sky Survey Atlas* to measure gas densities near ∼1800 OB stars within ∼400 pc of the Sun, obtaining a density PDF that resembles an LN function for densities in the range $0.1 < n < 10$ cm$^{-3}$. Wada et al. (2000) showed that the PDF of H I column density in the Large Magellanic Cloud (LMC) is approximately LN (at ∼15 pc resolution) over approximately two orders of magnitude. More recently, Berkhuijsen & Fletcher (2008) derived average volume densities in the diffuse (i.e., $n < 1$ cm$^{-3}$) ionized and atomic gas for sightlines toward ∼200 pulsars and ∼400 stars within a few kpc of the Sun. The resulting density PDFs were consistent with an LN function over ∼2 dex, but the precise shape of the PDF (i.e., the dispersion and density corresponding to the distribution peak) varied with Galactic latitude. Over larger scales, neither the density nor column density distribution of molecular hydrogen has been widely investigated. In part, this is because observations of $^{12}$CO($J = 1 \rightarrow 0$) emission—the most widely used tracer of extragalactic molecular gas—have been limited to low-resolution surveys of whole galaxies or high-resolution (often interferometric) imaging over a small fraction of a galactic disk. On much smaller scales, the PDF of $H_2$ column density has been examined for individual molecular clouds in the solar neighborhood, mostly through extinction of background stars (e.g., Kainulainen et al. 2009; Froebrich & Rowles 2010). These studies have shown that the column density PDFs of non-star-forming clouds are approximately LN, but that star-forming clouds exhibit power-law tails at high column densities, presumably due to the formation of high-density regions undergoing localized collapse.

Our aim in this paper is to provide a quantitative description of the properties of the CO emission in our high angular resolution survey of M51's inner disk (Plateau de Bure Arcsecond Whirlpool Survey (PAWS); Schinnerer et al. 2013), in order to provide simple empirical benchmarks for models of the $H_2$ content of galactic disks (e.g., Tasker & Tan 2009; Dobbs et al. 2011). For this purpose, we present PDFs of CO-integrated intensity and brightness temperature in M51, M33, and the LMC, as well as CO PDFs for different dynamical environments within the PAWS field. The extent to which the CO emission in M51 can be attributed to discrete, self-gravitating structures akin to giant molecular clouds (GMCs) in the Milky Way is discussed elsewhere (Colombo et al. 2013a). The rest of this paper is organized as follows. We summarize the origin and characteristics of the CO data sets that we have used in Section 2. Our method for constructing the PDFs is outlined in Section 3 and our results are presented in Section 4. Our discussion in Section 5 focuses on the relationship between PDFs constructed from our CO observations on ∼40 pc scales and the PDFs of $H_2$ density and column density predicted by numerical models and on the connection among GMC properties, SF, and the shape of the PDF for different M51 environments. We conclude with a summary of our key results in Section 6. We include three appendices, where we describe how we tested the robustness of the PDFs to non-physical effects such as resolution, sensitivity, and signal identification, and assessed the uncertainty associated with our estimates for the slopes of the GMC and young stellar cluster mass distributions.

## 2. DATA

### 2.1. M51

The CO data for M51 were obtained by PAWS (Schinnerer et al. 2013). PAWS observations mapped a total field of view of approximately 270″ × 170″ in the inner disk of M51 in the ABCD configurations of the PdBI between 2009 August and 2010 March. Since an interferometer filters out low spatial frequencies, the PdBI data were combined with

observations of CO emission in M51 obtained using the IRAM 30 m single-dish telescope in 2010 May. In this section, we summarize the most important aspects of the observations and data reduction; the PAWS observing strategy, data reduction and combination procedures, and flux calibration are described in detail by Pety et al. (2013).

#### 2.1.1. PdBI Observations

The PdBI observations consisted of two 30 field mosaics, centered such that their combination covers the inner part of M51. The mosaic pointings follow a hexagonal pattern, with each pointing being separated from its nearest neighbors by the primary beam full width at half maximum (FWHM). Each pointing was observed for $3 \times 15$ s in turn, allowing us to cycle completely through one mosaic pattern between calibrations, which were obtained every 22.5 minutes. The hexagonal pattern ensures Nyquist sampling along the declination axis but slightly undersamples the beam along the right ascension axis. The total telescope time in all four array configurations was 169 hr. The total on-source integration time during which useful data were obtained was 126.5 hr.

For the PAWS observations, the two polarizations of the PdBI's single-sideband receiver were tuned to 115.090 GHz, i.e., the $^{12}$CO($J = 1 \rightarrow 0$) rest frequency redshifted to the local standard of rest (LSR) velocity (471.26 km s$^{-1}$) of M51. Four correlator bands of 160 MHz per polarization were concatenated to cover a total bandwidth of 550 MHz, corresponding to a velocity bandwidth of 1430 km s$^{-1}$. The intrinsic frequency (velocity) channel spacing was 1.25 MHz (3.25 km s$^{-1}$). We later smoothed the data to a velocity resolution of 5 km s$^{-1}$ to reduce the effect of correlation between adjacent frequency channels and increase signal-to-noise. Inspection of the data showed CO emission between $\pm$110 km s$^{-1}$ of M51's systemic velocity. We therefore imaged and deconvolved $120 \times 5$ km s$^{-1}$ channels covering the LSR velocity range [174,769] km s$^{-1}$.

Calibration of the PdBI data was carried out using standard methods implemented in GILDAS/CLIC.[10] The bright ($\sim$10 Jy) quasars 0851+202 and 3C279 were used as bandpass calibrators. The temporal phase and amplitude gains were obtained from spline fits through regular measurements of the quasars 1418+546, 1308+326, and J1332+473. The flux scale was determined against the PdBI's primary flux calibrator, MWC349, and was found to be accurate to within $\sim$10%.

#### 2.1.2. IRAM 30 m Observations

CO emission in M51 was observed with the IRAM-30 m single dish telescope in order to recover the low spatial frequency information filtered out by the PdBI. A $\sim$60 square arcminute field, covering the entire M51 system, was mapped in position-switch on-the-fly observing mode. For this, we divided the survey field of view into seven regions. Four regions covered the central $400'' \times 400''$ of M51; the remaining three regions extended the coverage to include the ends of the spiral arms and M51's companion, NGC 5195. To suppress scan artifacts, each region was scanned in orthogonal directions, i.e., along the right ascension and declination axes, with each position in the central $400'' \times 400''$ observed 34 times on average. The slew speed was $8''$ s$^{-1}$ and the dump time was 0.5 s, yielding $\sim$5.5 integrations per beam in the scanning direction. The scanning rows were separated by $8''$, slightly oversampling the beam. We checked the pointing every hour and estimated the positional accuracy to be $\sim 2''$. Hot and cold loads plus the sky contribution were observed every 12 minutes to establish the temperature scale.

M51 observations were conducted with the EMIR receivers and WILMA autocorrelator backend to simultaneously record data for the $^{12}$CO($J = 1 \rightarrow 0$) and $^{13}$CO($J = 1 \rightarrow 0$) emission lines. We used the upper sideband for $^{12}$CO($J = 1 \rightarrow 0$), with a total bandwidth of 8 GHz. The channel spacing was 2 MHz, corresponding to a velocity channel spacing of 5.4 and 5.2 km s$^{-1}$ at 110 and 115 GHz, respectively.

The GILDAS/MIRA software was used to calibrate the temperature scale of the 30 m data. "OFF" spectra were constructed using GILDAS/MIRA's default scheme, i.e., averaging the closest (in time) observations together. These"OFF" spectra were then subtracted from the corresponding on-source spectra. Visual inspection indicated the presence of signal between $-200$ and +300 km s$^{-1}$ of M51's systemic velocity. A third-order polynomial was fit and subtracted from each spectrum. For the baseline fitting, we used an outlier-resistant approach and excluded regions of the spectrum that were known to contain bright emission, based on our inspection of trial data reductions or other observations. We experimented with higher- and lower-order baselines and found a third-degree fit to yield the best results. After fitting, we compared the rms noise about the baseline fit in signal-free regions of each spectrum with the expected theoretical noise. Based on this comparison, we rejected a small number of spectra where the observed noise was much greater than expected.

We gridded the calibrated, off-subtracted, baseline-subtracted spectra into a data cube with a pixel size of $4''$, weighting each spectrum by the inverse of the rms noise. For the gridding, we employed a Gaussian convolution kernel with a FWHM of $8''$. This gridding strategy increases the effective FWHM of the beamwidth to $\sim 23\farcs5$ at 115 GHz. After gridding, we fit and subtracted a second set of third-order polynomial baselines from each spectrum; this procedure was a minor refinement to the initial (pre-gridding) baseline fit.

#### 2.1.3. Combination of Single-dish and Interferometric Data

The final PAWS data cube is a joint deconvolution of the PdBI and IRAM 30 m data sets. The short-spacing visibilities not sampled by the PdBI were recreated from the single-dish map using the GILDAS/MAPPING software. For this, the map was deconvolved from the IRAM 30 m beam in the Fourier plane before multiplication by the PdBI primary beam in the image plane (as described by Rodriguez-Fernandez et al. 2008). After a further Fourier transform, pseudo-visibilities were sampled between 0 and 15 m (the diameter of a PdBI antenna) and these visibilities were then merged with the interferometric observations. For the joint deconvolution, we used an adaption of the Högbom CLEAN algorithm, as implemented in GILDAS/MAPPING. Supports defining the region to search for CLEAN components were defined for each velocity channel, based on where significant emission was detected in the 30 m cube. The convergence of the deconvolution was checked in three different ways. First, the cumulative flux as a function of the number of CLEAN components converged in each channel. Second, the residual channel images look like noise. Both criteria indicate a satisfying convergence of the deconvolution. Finally, we deconvolved the data a second time using exactly the same method except that we doubled the maximum number of CLEAN components from 320,000 to 640,000. The subtraction of both cubes again looks like noise.

[10] See http://www.iram.fr/IRAMFR/GILDAS for more information about the GILDAS software (Pety 2005).

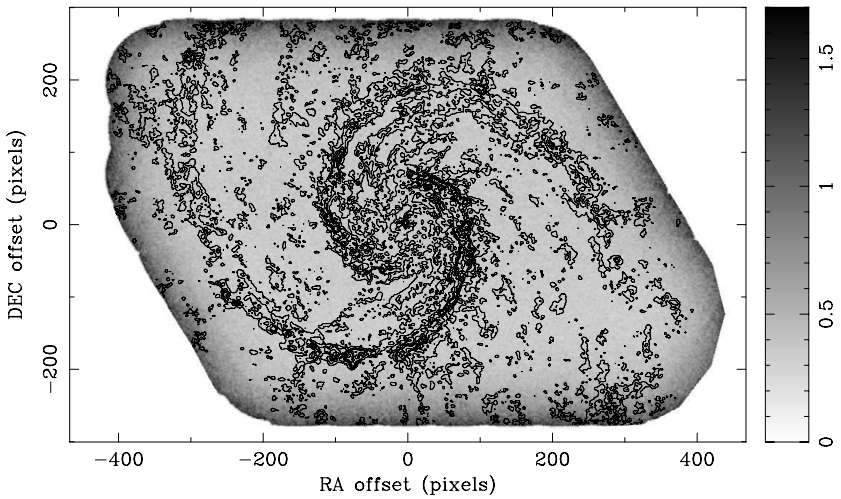


**Figure 1.** rms of the noise fluctuations across the PAWS survey region. The grayscale image is shown in units of $T_{\rm mb}$ K. The black contours indicate $I({\rm CO}) = 20$, 70, 120, 170, 220, 320, and 320 K km s$^{-1}$, as measured by PAWS.

The effective angular resolution of the final combined PAWS data cube is $1\farcs16 \times 0\farcs97$, corresponding to a spatial resolution of ∼40 pc at our assumed distance to M51 (7.6 Mpc; Ciardullo et al. 2002). The data cube covers the LSR velocity range 173–769 km s$^{-1}$ and the width of each velocity channel is 5 km s$^{-1}$. The mean rms of the noise fluctuations across the survey is $\sigma_{\rm rms} \sim 0.4$ K in a 5.0 km s$^{-1}$ channel. For a typical CO linewidth of 15 km s$^{-1}$, this corresponds to an average sensitivity of 3.5 K km s$^{-1}$ for the map of CO-integrated intensity. A map of the noise fluctuations across the PAWS field, overlaid with contours of CO-integrated intensity, is shown in Figure 1.

### 2.2. M33

For M33, we use the CO data presented by Rosolowsky et al. (2007), which combine observations by BIMA (Engargiola et al. 2003) and FCRAO (Heyer et al. 2004). The common field of view of the single-dish and interferometer surveys is 0.25 deg$^2$, covering most of M33's optical disk. The angular resolution of the combined cube is $13\farcs2 \times 12\farcs9$, corresponding to a spatial resolution of 53 pc for our assumed distance to M33 of 840 kpc (e.g., Galleti et al. 2004). The data cover the LSR velocity range [−400, 40] km s$^{-1}$and the velocity channel width is 2.0 km s$^{-1}$. The average rms noise per channel is 0.24 K.

### 2.3. The Large Magellanic Cloud

The CO data for the LMC were obtained by the Magellanic Mopra Assessment (MAGMA). The MAGMA survey design, data acquisition, reduction procedures, and calibration are described in detail by Wong et al. (2011). MAGMA mapped CO cloud complexes that had been identified at lower resolution by NANTEN (Fukui et al. 2008), targeting 114 NANTEN GMCs with CO luminosities higher than 7000 K km s$^{-1}$ pc$^2$and peak integrated intensities greater than 1 K km s$^{-1}$. The combined field of view of the MAGMA survey is ∼3.6 deg$^2$. Although the clouds targeted for mapping represent only ∼50% of the clouds in the NANTEN catalog, the region surveyed by MAGMA contributes ∼80% of the total CO flux measured by NANTEN. The MAGMA LMC data cube has an effective resolution of 45″, corresponding to a linear resolution of ∼11 pc at the distance of the LMC (50.1 kpc; Alves 2004). The velocity channel width is 0.53 km s$^{-1}$and the total LSR velocity range of the cube is 200–305 km s$^{-1}$. The average rms noise per channel across the MAGMA field is 0.3 K.

## 3. METHODS

### 3.1. CO Probability Distribution Functions

We construct PDFs of CO-integrated intensity $I({\rm CO})$ and CO brightness $T_{\rm mb}$. The $I({\rm CO})$ PDF is simply a histogram of the $(x, y)$ pixel values within a $I({\rm CO})$ map, while the $T_{\rm mb}$ PDF is a histogram of the $(x, y, v)$ pixel values within a spectral line cube. The PDFs are constructed after applying a blanking mask that identifies genuine emission within the data cubes. For our analysis of the PAWS data cube, we identify significant emission using the masking method described by Pety et al. (2013). For our comparative analysis of M51, M33, and the LMC in Section 4.4, we construct an initial mask that contains pixels above a $5\sigma_{\rm rms}$ threshold over two or more contiguous velocity channels. This mask defines a high significance core, which is then expanded to include all connected pixels above $1.2\sigma_{\rm rms}$ over at least two velocity channels. We discuss the rationale for using these blanking masks and the influence of different masking techniques on the shape of the PDFs in Appendix A. The total number of independent data points within the $I({\rm CO})$ PDFs varies between ∼15,000 and ∼250,000 (for the $T_{\rm mb}$ PDFs, this increases by factor of ∼7). For the $I({\rm CO})$ PDFs, we normalize the histogram by the number of pixels within the survey field of view, not by the number of pixels where significant emission is detected. Likewise, we normalize the $T_{\rm mb}$ histogram by the number of independent $(x, y, v)$ elements in the data cube.

As we discuss in Section 4.3, the PDFs of CO-integrated intensity and CO brightness $T_{\rm mb}$ within M51 exhibit diverse shapes that are often inconsistent with a simple functional form such as a LN or power-law distribution. We therefore parameterize the shape of each PDF using the brightness distribution index (BDI), a metric recently devised by Sawada et al. (2012b) to characterize the ratio between faint and bright $^{12}{\rm CO}(J = 1 \rightarrow 0)$ emission within an $0\fdg8 \times 0\fdg8$ field in the Galactic plane. More precisely, we specify the BDI of CO brightness as

$$\mathrm{BDI} = \log\left(\frac{\sum_{T_2<T_i<T_3} T_i}{\sum_{T_0<T_i<T_1} T_i}\right), \quad (1)$$

where $T_i$ is the brightness of the $i$th pixel and $(T_0, T_1, T_2, T_3) = (1.2, 2.5, 5, \infty)$ K are the thresholds that we use to define faint and bright emission. These are not the same thresholds adopted by Sawada et al. (2012b) for their analysis at $\lesssim$1 pc resolution, but are chosen such that variations in the shape of the PDF are captured (i.e., BDI is defined) for all the M51 environments that we analyze and that all the pixels included in the calculation contain significant CO emission (i.e., $T_i > 3\sigma_{\rm rms}$). We define an equivalent parameter for the $I$(CO) PDFs, which we refer to as the integrated intensity distribution index (IDI). Analogous to Equation (1), we specify this as

$$\mathrm{IDI} = \log\left(\frac{\sum_{I_2<I_i<I_3} I_i}{\sum_{I_0<I_i<I_1} I_i}\right), \quad (2)$$

adopting $(I_0, I_1, I_2, I_3) = (10.5, 25, 60, \infty)$ K km s$^{-1}$.

When appropriate, we derive the best-fitting LN function to a PDF using a Levenberg–Marquardt fit to the function:

$$P(s) = c_0 \times \exp\left[\frac{-(\log s - \log s_0)^2}{2x^2}\right]. \quad (3)$$

We define the probability $P(s)$ as the number of pixels in the bin divided by the total number of pixels in the map (or cube). Depending on context, $s$ represents $I$(CO) or $T_{\rm mb}$. Only bins to the right of the peak of the PDF, brighter than $4\sigma_{\rm rms}$ and containing 10 or more pixels, are used to derive the fit. Several of the PDFs resemble power laws more than LN functions. In this case, we estimate the best-fitting slope of the power law using ordinary least squares linear regression.

### 3.2. Identifying and Parameterizing GMC Properties

In Section 5.2, we investigate whether there is a connection between the shape of the CO PDFs and the properties of GMCs identified within the PAWS field. For this, we use the GMC catalog presented by Colombo et al. (2013a). The catalog was constructed using the CPROPS package (Rosolowsky & Leroy 2006, hereafter RL06). CPROPS uses a dilated mask technique to isolate regions of significant emission within spectral line cubes and a modified watershed algorithm to assign the emission into individual clouds. Moments of the emission along the spatial and spectral axes are used to determine the size, linewidth, and flux of the clouds.

To generate the PAWS GMC catalog, CPROPS first identifies significant emission by finding pixels with CO brightness $T_{\rm mb}$ above a $4\sigma_{\rm rms}$ threshold across two adjacent velocity channels, where the rms noise $\sigma_{\rm rms}$ is estimated from the median absolute deviation of each spectrum. This mask is then expanded to include all connected pixels with $T_{\rm mb} > 1.5\sigma_{\rm rms}$. Emission regions are then decomposed into GMCs by identifying emission that can be uniquely associated with local maxima. Full details of the decomposition procedure are presented in Colombo et al. (2013a).

We adopt the default CPROPS definitions of GMC properties. The cloud radius is defined as $R = 1.91\sigma_{\rm R}$ pc, where $\sigma_{\rm R}$ is the geometric mean of the second moments of the emission along the cloud's major and minor axes. The velocity dispersion $\sigma_{\rm v}$ is the second moment of the emission distribution along the velocity axis, which for a Gaussian line profile is related to the FWHM linewidth, $\Delta v$, by $\Delta v = \sqrt{8\ln 2}\sigma_{\rm v}$. The CO luminosity of the cloud $L_{\rm CO}$ is the emission inside the cloud integrated over position and velocity, i.e.,

$$L_{\rm CO}\ [\mathrm{K\,km\,s^{-1}\,pc^2}] = D^2\left(\frac{\pi}{180\times 3600}\right)^2 \Sigma T\,\delta v\delta x\delta y\ , \quad (4)$$

where $D$ is the distance to the galaxy in pc, $\delta x$ and $\delta y$ are the spatial dimensions of a pixel in arcseconds, and $\delta v$ is the width of one channel in km s$^{-1}$. The mass of molecular gas estimated from the GMC's CO luminosity $M_{\rm CO}$ is calculated as

$$M_{\rm CO}\ [M_\odot] \equiv 4.4\frac{X_{\rm CO}}{2\times 10^{20}[\,\mathrm{cm^{-2}\,(K\,km\,s^{-1})^{-1}}]}L_{\rm CO}\ , \quad (5)$$

where $X_{\rm CO}$ is the assumed CO-to-H$_2$ conversion factor and a factor of 1.36 is applied to account for the mass contribution of helium. The fiducial value of $X_{\rm CO}$ used by CPROPS is $X_{\rm CO} = 2.0\times 10^{20}$ cm$^{-2}$ (K km s$^{-1}$)$^{-1}$. The virial mass is estimated as $M_{\rm vir}\ [M_\odot] = 1040\sigma_{\rm v}^2 R$, which assumes that molecular clouds are spherical with truncated $\rho \propto r^{-1}$ density profiles (MacLaren et al. 1988). CPROPS estimates the error associated with a cloud property measurement using a bootstrapping method, which is described in Section 2.5 of RL06.

The final PAWS GMC catalog contains 1507 objects. The GMCs have peak brightness temperatures between ~2 and 16 K, radii between 5 and 150 pc, and velocity dispersions between 1 and 30 km s$^{-1}$. The catalog and the properties of GMCs in different environments within the PAWS field are the subject of a companion paper (Colombo et al. 2013a). In general, the physical properties of the cataloged GMCs are similar to the GMCs identified by CO surveys of the inner Milky Way and other nearby galaxies, although GMCs in M51 tend to be larger, brighter, and have higher velocity dispersions and mass surface densities relative to their sizes than the GMCs in nearby low-mass systems such as the Magellanic Clouds and M33 (Hughes et al. 2013). The spatial resolution and sensitivity of PAWS is sufficient to resolve structures with size and mass comparable to a typical Galactic GMC (50 pc, $10^5\ M_\odot$; Blitz 1993). We note, however, that CO emission is almost ubiquitous across the PAWS field and that much of the emission resides in large (~kpc-sized) regions of high brightness that bear little resemblance to Galactic GMCs. Overall, the cataloged GMCs account for approximately half of the total CO flux within the PAWS data cube, a fraction that varies from ~40% in the interarm region to ~60% in the spiral arms and central zone.

## 4. RESULTS

### 4.1. $I$(CO) PDF

The PDF of CO-integrated intensity for the entire PAWS field is presented in Figure 2(a). The distribution is adequately described by an LN function, with a mean of $\langle I(\mathrm{CO})\rangle = 21.6$ K km s$^{-1}$ and a logarithmic width of 0.44. The logarithmic dispersion in the fit residuals $\epsilon$ for bins above the $3\sigma$ sensitivity limit that contain more than five counts is 0.08. Relative to this LN function, there is some evidence for a truncation at high $I$(CO) values ($\gtrsim$200 K km s$^{-1}$). In principle, this could be due to the opacity of the $^{12}$CO($J = 1 \rightarrow 0$) emission line, an effect that is often observed on pc scales in regions of high extinction ($A_{\rm V} \gtrsim$ 5–10 mag; e.g., Lombardi et al. 2006; Pineda et al. 2008), but has rarely been considered for the scales probed by extragalactic observations (cf. Dickman et al. 1986). Against this interpretation, the 99th percentile of the CO peak brightness within the PAWS field is only ~7 K, suggesting that there are

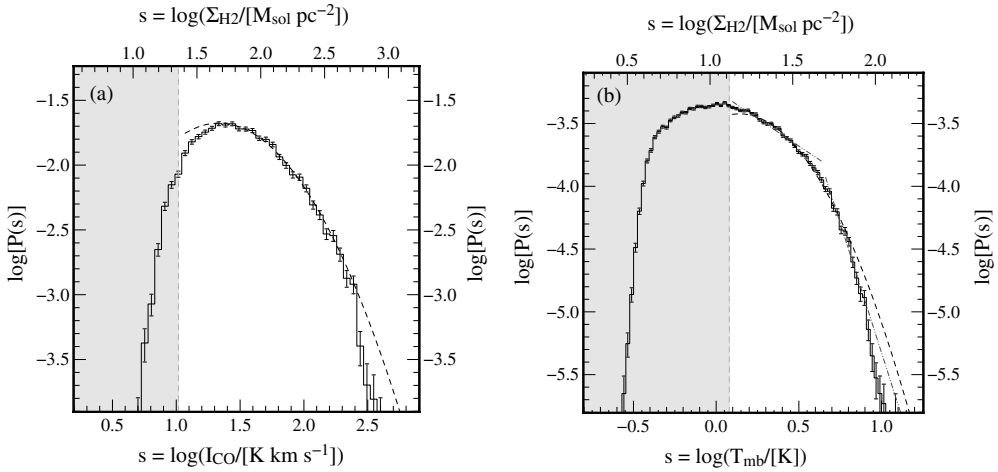


**Figure 2.** (a) $I$(CO) and (b) $T_{\rm mb}$ PDFs for emission within the PAWS field. In both panels, the dashed parabola indicates the LN function that provides the best fit to the PDF. In panel (b), the dot-dot-dashed lines represent two segments of a broken power law, which also provides a reasonable fit to the distribution. The gray shaded region indicates values beneath our nominal $3\sigma_{\rm rms}$ sensitivity limits of 10.5 K km s$^{-1}$ (panel (a)) and 1.2 K (panel (b)). The top horizontal axis shows the equivalent $H_2$ mass surface density for the $I$(CO) or $T_{\rm mb}$ value on the lower axis, assuming $X_{\rm CO} = 2 \times 10^{20}$ cm$^{-2}$ (K km s$^{-1}$)$^{-1}$ and a helium contribution of 1.36 by mass. The vertical error bars represent the uncertainty associated with simple counting ($\sqrt{N}$) errors.

negligible sightlines where the CO emission completely fills the telescope beam. Furthermore, recent numerical simulations that examine the ability of $I$(CO) to trace the $H_2$ column density on 20–60 pc scales show that saturation tends to produce a secondary peak in the $I$(CO) PDF rather than a smooth truncation (Shetty et al. 2011; Feldmann et al. 2012; see also Section 5.4). The finite resolution of observational data can also produce a truncation at high intensities (we explore this effect in Appendix B). In this case, however, we would expect the $I$(CO) PDFs for subregions within the PAWS field to exhibit similar thresholds, whereas several of them are consistent with pure LN functions (see Section 4.3).

The truncation of the PDF is Figure 2(a) may therefore be physical. Elmegreen (2011) show that the density PDF should fall beneath a pure LN function at high gas densities if the Mach number decreases with increasing average gas density (as would be expected for a cloud that obeys the Larson (1981) size–linewidth relation). Alternatively, the truncation may reflect the efficacy of feedback processes that prevent the molecular gas from reaching very high mass surface densities ($\Sigma_{\rm H_2} \gtrsim 400\ M_\odot$ pc$^{-2}$, assuming $X_{\rm CO} = 2.0 \times 10^{20}$ cm$^{-2}$ (K km s$^{-1}$)$^{-1}$). We discuss physical processes that could be influencing the shape of the $I$(CO) PDFs in M51 in more detail in Section 5.4.

### 4.2. $T_{mb}$ PDF

The PDF of CO brightness for the PAWS cube is shown in Figure 2(b). The $T_{\rm mb}$ PDF is less like an LN function than the $I$(CO) PDF, with two roughly flat segments across $1 < T_{\rm mb} < 3$ K and $T_{\rm mb} > 5$ K. Our LN fit to the PDF yields a mean $\langle T_{\rm mb} \rangle \sim 1.4$ K and logarithmic width $x \sim 0.3$. Assuming that the true distribution of $T_{\rm mb}$ values is LN, there are fewer high-brightness pixels than would be expected from this LN function. The truncation begins to occur at a CO brightness temperature of ∼5 K, which would seem too low to be due to opacity effects. Instead of an LN function, a broken power law with a slope of ∼−0.9 for $1 < T_{\rm mb} < 5$ K and a much steeper slope of ∼−4.1 for $T_{\rm mb} > 5$ K—or, alternatively, a pure power law with a truncation at ∼5 K—may provide a better description of the PDF. The fit parameters and goodness of fit for the best-fitting LN and power-law functions to the $T_{\rm mb}$ PDF in Figure 2(b) are listed in Table 1.

### 4.3. M51 Environments

An important question that we would like to address with the PAWS data is whether the organization and physical properties of molecular gas depend on galactic environment. Variations in the shape of the PDF could reflect differences in the relative importance of self-gravity, SF feedback, or gas flows in different parts of the galactic disk, which in turn might influence the ability of the molecular gas to form stars. Within the PAWS field, there are three main regions where the gas is likely to experience distinct physical conditions: within the strong spiral arms, the interarm region situated upstream and downstream of the spiral arms, and the central region, where the gas is influenced by the presence of a nuclear stellar bar (Zaritsky et al. 1993). These regions can be further classified according to their level of SF activity (as traced by, e.g., H$\alpha$) and/or gas flows, which we determine using the present-day torque profile (Meidt et al. 2013).

Here, we analyze seven regions within the PAWS field where we expect the molecular gas to experience different dynamical effects (see Figure 3). We define the different spiral arm regions according to the direction of gas flows driven in response to the underlying gravitational potential, which we derive from a map of M51's stellar mass distribution (Meidt et al. 2012). The widths of the spiral arms are defined with respect to the observed gas kinematics. We determine the zone of enhanced spiral streaming centered around the arm by measuring the (rotational) auto-correlation of azimuthal streaming velocities in the PAWS field (Colombo et al. 2013b). We construct azimuthal profiles of the auto correlation signal in a series of radial bins and take the width of the signal at 95% maximum as our measure of the kinematic arm width. The average kinematic width from along the two arms is centered on the spiral arm ridge line, defined by eye using the PAWS map of CO peak brightness. Both the location of the ridge and the width are assumed to be symmetric. The interarm region is divided into upstream and downstream by the midpoint of the spiral arm ridge lines. The definition of the spiral arm regions is based on the identification of distinct spiral patterns within the galactic disk (cf. Vogel et al. 1993; Shetty et al. 2007; Meidt et al. 2008; Dobbs et al. 2010) that we refined and describe in detail elsewhere (Meidt et al. 2013; Colombo et al. 2013b).

**Table 1**
Fit Parameters for CO PDFs in M51, M33, the LMC, and Environments within M51

| LN Fits | | | | | |
|---|---|---|---|---|---|
| Figure | CO Property | Galaxy/Region | Mean | Logarithmic Width | Goodness of Fit |
| | | | $s_0$ | $x$ | $\epsilon$ |
| 2(a) | $I$(CO) | PAWS field | 21.6 K km s$^{-1}$ | 0.44 | 0.08 |
| 2(b) | $T_{mb}$ | PAWS field | 1.4 K | 0.31 | 0.18 |
| 4(a) | $I$(CO) | Bar | 50.5 K km s$^{-1}$ | 0.21 | 0.41 |
| 4(b) | | Ring | 40.8 K km s$^{-1}$ | 0.47 | 0.18 |
| 4(c) | | A1I | 23.8 K km s$^{-1}$ | 0.47 | 0.20 |
| 4(d) | | A1O | 36.6 K km s$^{-1}$ | 0.35 | 0.08 |
| 4(e) | | A1 | 27.4 K km s$^{-1}$ | 0.44 | 0.28 |
| 4(f) | | A2 | 25.4 K km s$^{-1}$ | 0.35 | 0.10 |
| 4(g) | | Up | 18.8 K km s$^{-1}$ | 0.25 | 0.09 |
| 4(h) | | Down | 24.0 K km s$^{-1}$ | 0.22 | 0.13 |
| 5(a) | $T_{mb}$ | Bar | 1.5 K | 0.30 | 0.11 |
| 5(b) | | Ring | 1.6 K | 0.37 | 0.19 |
| 5(c) | | A1I | 1.0 K | 0.38 | 0.17 |
| 5(d) | | A1O | 1.5 K | 0.29 | 0.17 |
| 5(e) | | A1 | 1.3 K | 0.32 | 0.20 |
| 5(f) | | A2 | 1.2 K | 0.31 | 0.10 |
| 5(g) | | Up | 1.1 K | 0.24 | 0.05 |
| 5(h) | | Down | 1.0 K | 0.29 | 0.06 |
| 6(a) | $I$(CO) | M51 | 12.3 K km s$^{-1}$ | 0.53 | 0.10 |
| 6(c) | | LMC | 1.8 K km s$^{-1}$ | 0.26 | 0.13 |
| 6(d) | $T_{mb}$ | M51 | 0.8 K | 0.36 | 0.32 |
| 6(f) | | LMC | 0.1 K | 0.28 | 0.14 |

| Power-law fits | | | | | | |
|---|---|---|---|---|---|---|
| Figure | CO Property | Galaxy/Region | Slope | Slope 2 | Domain | Goodness of Fit |
| | | | $\gamma_1$ | $\gamma_2$ | | $\epsilon$ |
| 2(b) | $T_{mb}$ | PAWS field | −0.88 | −4.13 | $\gamma_1$ : [1 < $T_{mb}$ < 3] K<br>$\gamma_2$ : [5 < $T_{mb}$ < 8] K | 0.10 |
| 4(c) | $I$(CO) | A1I | −0.85 | ... | $\gamma_1$ : $I$(CO) > 10 K km s$^{-1}$ | 0.24 |
| 5(b) | $T_{mb}$ | ring | −0.53 | −6.26 | $\gamma_1$ : [1 < $T_{mb}$ < 5] K<br>$\gamma_2$ : [8 < $T_{mb}$ < 12.5] K | 0.09 |
| 5(c) | | A1I | −0.97 | −4.68 | $\gamma_1$ : [1 < $T_{mb}$ < 4] K<br>$\gamma_2$ : [5 < $T_{mb}$ < 8] K | 0.07 |
| 5(d) | | A1O | −0.96 | −4.97 | $\gamma_1$ : [1 < $T_{mb}$ < 4] K<br>$\gamma_2$ : [5 < $T_{mb}$ < 8] K | 0.07 |
| 5(e) | | A1 | −0.97 | −4.82 | $\gamma_1$ : [1 < $T_{mb}$ < 4] K<br>$\gamma_2$ : [5 < $T_{mb}$ < 8] K | 0.08 |
| 6(d) | $T_{mb}$ | M51 | −1.30 | −4.96 | $\gamma_1$ : [1 < $T_{mb}$ < 3] K<br>$\gamma_2$ : [5 < $T_{mb}$ < 8] K | 0.15 |
| 6(e) | | M33 | −3.63 | ... | $\gamma_1$ : [0.8 < $T_{mb}$ < 1.3] K | 0.13 |
| 6(f) | | LMC | −2.15 | ... | $\gamma_1$ : [0.2 < $T_{mb}$ < 1] K | 0.07 |

**Notes.** Parameters of best-fitting functions to PDFs in Figures 2, 4, 5, and 6. The parameters of the LN functions are determined from a Levenberg–Marquardt fit to Equation (3); the power-law and broken power-law fits are estimated using ordinary least squares regression. We use the logarithmic dispersion of the fit residuals to estimate the goodness of fit.

The seven zones that we use to conduct our analysis are as follows.

1. *Nuclear bar.* The region at galactocentric radii $R < 23''$. The boundary is defined by the bar corotation resonance, inside of which the bar exerts negative torques and drives gas radially inward.
2. *Molecular ring.* The region $23 < R < 35''$. Here, the gas is influenced by both the bar and innermost spiral arms. Outside the bar corotation resonance, gas is driven radially outward, while the spiral drives gas radially inward inside its own corotation. These opposing torques accumulate gas in a ring-like structure. The region hosts some of the most active high-mass SF in M51.
3. *Inner density-wave spiral arm.* The arm region $35 < R < 55''$. The inner boundary is defined by the molecular ring and the outer boundary is the corotation radius of the density-wave spiral arms. Within this zone, gas is driven radially inward by negative spiral arm torquing. Despite the high gas surface densities in this region, there is little SF—as traced by H$\alpha$ and 24 $\mu$m emission—that is directly associated with the brightest CO emission (Schinnerer et al. 2013).
4. *Outer density-wave spiral arm.* The arm region $55 < R < 85''$. This region extends from the density-wave corotation resonance to the start of the material spiral. Within this zone, gas is driven radially outward by positive spiral arm torquing.

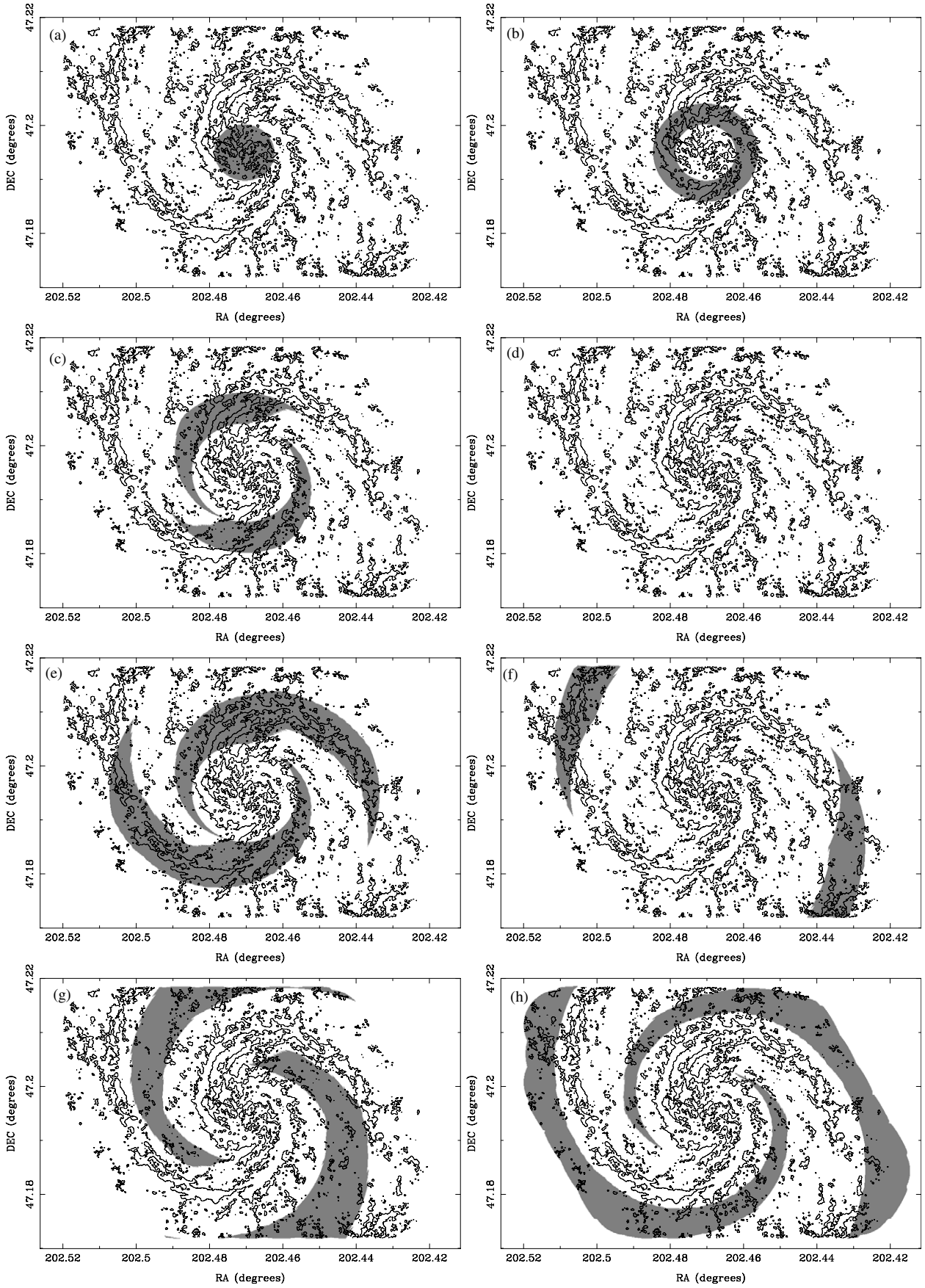


**Figure 3.** Different environments within the PAWS field that we analyze in this paper, indicated using gray shading in each panel. (a) Nuclear bar (bar); (b) molecular ring (ring); (c) first spiral pattern inside corotation (A1I); (d) first spiral pattern outside corotation (A1O); (e) first spiral pattern (density wave arm, A1); (f) second spiral pattern (material arm, A2); (g) interarm region upstream of the spiral arms (up); and (h) interarm region downstream of the spiral arms (down). The black contours in all panels indicate $I(\mathrm{CO}) = 25$ K km s$^{-1}$, as measured by PAWS.

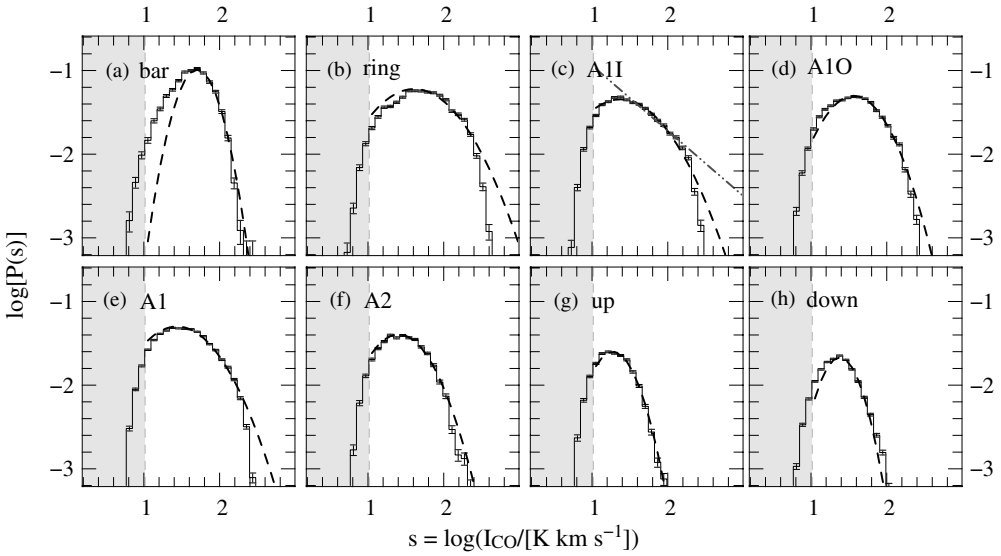


**Figure 4.** $I$(CO) PDFs for different regions within the PAWS field. The gray shaded region represents values beneath our nominal $3\sigma_{\rm rms}$ sensitivity limit of 10.5 K km s$^{-1}$. Where an LN (power-law) function provides a good description of the PDF, it is indicated by a dashed (dot–dashed) line. The vertical error bars represent the uncertainty associated with simple counting ($\sqrt{N}$) errors.

5. *Material spiral arm.* The arm region $R > 85''$. This region extends from the boundary of positive arm torques associated with the density wave spiral to the edge of the PAWS field. There is some indication that gas flows radially inward in this zone.
6. *Interarm region, downstream of the spiral arms.*
7. *Interarm region, upstream of the spiral arms.*

Finally, we note that the projected area of the seven regions is still quite large (between ∼2 and 17 kpc$^2$) and each contains a statistically significant number of GMCs ($\gtrsim$100). The PDFs of CO emission in these regions are therefore more comparable with the PDFs of simulated galactic disks than the PDFs of individual clouds.

Figure 4 shows that the $I$(CO) PDFs for different M51 environments exhibit diverse shapes. The panels of Figure 4 are ordered such that the PDF amplitudes decrease from top left to bottom right, which reflects the fact that CO emission is more prevalent in the arms and central region of M51 than in the interarm region. The PDFs also tend to decrease in width, indicating that the fraction of pixels with bright CO emission declines with the overall frequency of CO detections. The PDFs of the spiral arms are notably wider than for the interarm environments; it is also evident that the PDF corresponding to the first spiral pattern (A1, i.e., the density wave spiral arm) is wider than the PDF for the second spiral (A2, the material arm). Since $I$(CO) is the integral of the CO brightness over the line profile, this variation in the PDF width would seem consistent with the results of previous studies (e.g., Garcia-Burillo et al. 1993; Kuno & Nakai 1997; Aalto et al. 1999; Schuster et al. 2007) that find that the average CO-integrated intensity and CO linewidth decreases with increasing distance along the arms and from the arm to the interarm region.

The differences in the width of the PDFs among M51 environments are reflected in the IDI values that we derive, which become more positive as the number of pixels with $I$(CO) $>$ 60 K km s$^{-1}$ increases (see Table 2). The development of more high-brightness emission appears to be accompanied by a change in the PDF shape: an LN function is a better description of the PDFs in the interarm region than in the spiral arm and ring regions. The $I$(CO) PDFs for the first spiral pattern, especially inside corotation (A1I), appear more like broken or truncated power laws than LN functions. The PDFs in the center of M51 also diverge from an LN shape: the $I$(CO) distribution in the molecular ring is essentially flat between ∼20 and 150 K km s$^{-1}$, while the PDF of the bar is the only region with an unambiguous decline at low intensities ($I$(CO) $\lesssim$ 50 K km s$^{-1}$). Several PDFs appear truncated near $I$(CO) $\sim$ 300 K km s$^{-1}$; this is seen most clearly in the molecular ring, but the distributions in the first spiral arm regions also decline steeply for $I$(CO) $\gtrsim$ 300 K km s$^{-1}$.

In Figure 5, we present the PDFs of CO brightness for the different M51 environments. The distributions are more uniform than those of integrated intensity, but variations similar to those identified for the $I$(CO) PDFs are still evident. The PDF amplitude tends to decrease from panels (a) to (h) and only the interarm regions and second spiral arm (A2) yield PDFs that are approximately LN across the observed range of $T_{\rm mb}$ values (see Table 1). As noted for the $I$(CO) PDFs, regions with a relatively wide $T_{\rm mb}$ PDF (e.g., the ring, bar, and spiral arms)

**Table 2**
Brightness and Integrated Intensity Distribution Index for M51 Environments

| Region | $L_{\rm CO}$ ($10^7$ K km s$^{-1}$ pc$^2$) | BDI | IDI |
|---|---|---|---|
| Global | 70.4 | −0.66 | 0.40 |
| Nuclear bar | 6.6 | −0.85 | 0.76 |
| Molecular ring | 16.6 | −0.13 | 1.08 |
| Arm 1 inside corotation (A1I) | 11.9 | −0.59 | 0.52 |
| Arm 1 outside corotation (A1O) | 17.6 | −0.83 | 0.55 |
| Arm 1 (A1) | 29.6 | −0.72 | 0.54 |
| Arm 2 (A2) | 6.7 | −0.76 | 0.12 |
| Upstream | 4.7 | −1.73 | −0.95 |
| Downstream | 6.2 | −1.50 | −0.65 |

**Notes.** The total CO luminosity (Column 2), brightness distribution index (BDI, Column 3), and integrated IDI (Column 4) for the different M51 environments (see Figure 3). The BDI and IDI values are calculated according to Equations (1) and (2), respectively. More positive BDI and IDI values indicate PDFs that have a larger fraction of pixels at high CO intensities.

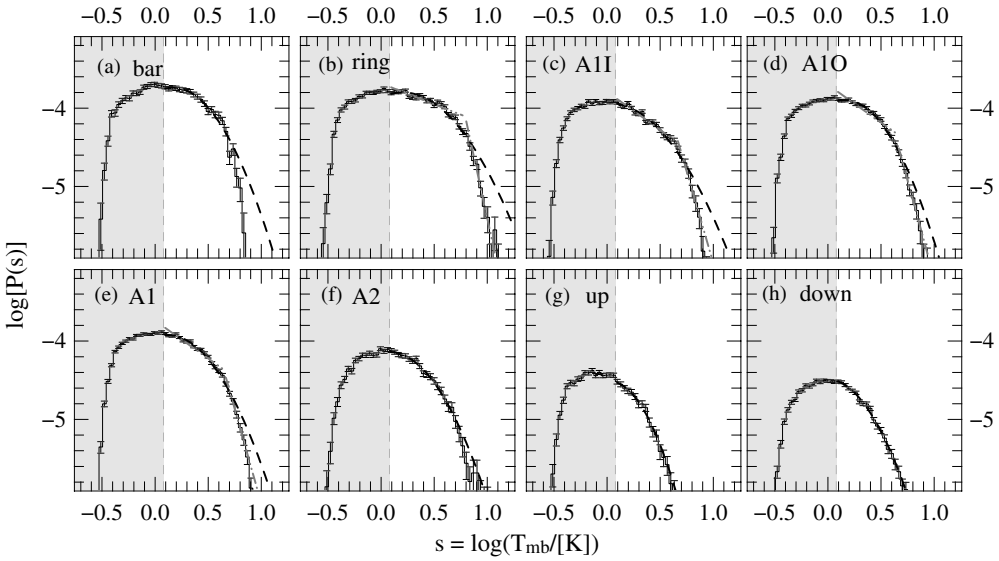


**Figure 5.** PDFs of CO brightness for different regions within the PAWS field. In each panel, the gray shaded region represents values beneath our nominal $3\sigma$ sensitivity limit of 1.2 K. When appropriate, the best-fitting LN (power-law) function is indicated by a dashed (dot–dashed) line. The vertical error bars represent the uncertainty associated with simple counting ($\sqrt{N}$) errors.

have more positive BDIs and also tend to diverge from an LN shape, in this case developing a pronounced change of slope near $T_{\rm mb} \gtrsim 6$ K. This effect is most clearly seen for the PDFs of the molecular ring (panel (b)) and the first spiral pattern inside corotation (panel (c)), but generally it appears that an increase in the fraction of high-brightness CO emission is associated with a PDF that more resembles a truncated power law than an LN function. We discuss this result in relation to similar trends observed for PDFs of CO emission in the Galaxy in Section 5.1.

### *4.4. Comparison among M51, M33, and the LMC*

Finally, we can compare the PDFs of CO-integrated intensity and CO brightness for the inner disk of M51 with the corresponding PDFs for other nearby galaxies. As we discuss in Appendix B, the shape of the PDF is sensitive to the resolution and sensitivity of the data. Prior to constructing the PDFs, we therefore degraded the M51 and LMC data cubes to the same spatial resolution as the M33 cube (∼53 pc) and folded the M33 and LMC data cubes along the velocity axis to the same channel width as the M51 cube (5 km s$^{-1}$). We interpolated all the cubes onto an $(x, y)$ grid with the same pixel dimensions in physical space (15 × 15 pc). Significant emission was identified according to the method outlined in Section 3. The resulting masks were applied to the original data cubes and the integrated intensity images were constructed by summing unblanked pixels across the full velocity bandwidth of each survey.

The PDFs obtained from the $I$(CO) maps of M33, the LMC and M51 are shown in the left panels of Figure 6. The shape of the $I$(CO) PDF for M33 is highly uncertain due to the modest sensitivity of the BIMA+FCRAO data cube. Nonetheless, it is obvious that CO emission in the LMC and M33 are alike in the sense that the maximum observed $I$(CO) intensities are ∼10 K km s$^{-1}$ at the resolution of our analysis and not a few times 100 K km s$^{-1}$, as observed for M51. The $I$(CO) PDF for the LMC appears to be well represented by a narrow LN function with mean $\langle I(\mathrm{CO})\rangle = 2$ K km s$^{-1}$and a logarithmic width $x = 0.3$. Since MAGMA is a targeted rather than a spatially complete survey of the LMC disk (see Section 2), the amplitude of its PDF is biased high compared with that of M51 and M33; normalizing by the full projected area of the LMC's

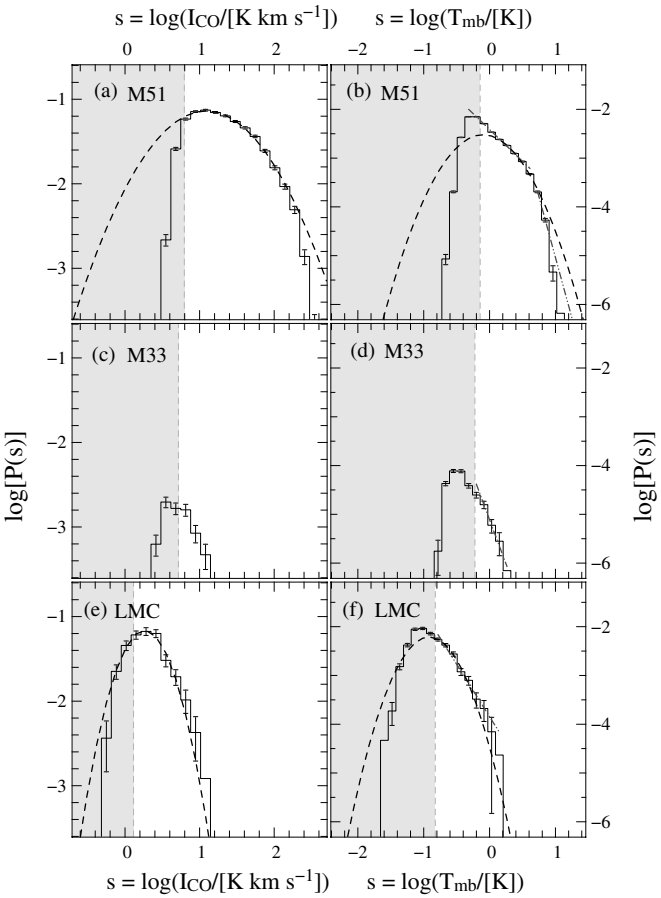


**Figure 6.** PDFs of $I$(CO) (panels (a)–(c)) and $T_{\rm mb}$ (panels (d)–(f)) for M51, the LMC, and M33, constructed using a dilated mask technique. The data sets have been smoothed to the same spatial scale and interpolated onto an $(x, y, v)$ grid with the same spatial and spectral dimensions. In all panels, the gray shaded region corresponds to pixels beneath the $3\sigma_{\rm rms}$ sensitivity limits of the individual data cubes. The vertical error bars represent the uncertainty associated with simple counting ($\sqrt{N}$) errors. Where relevant, the best-fitting LN (power-law) function is indicated by a dashed (dot–dashed) line.

H I disk, rather than the MAGMA field of view, would reduce the amplitude by more than an order of magnitude. The MAGMA survey strategy of targeting the brightest clouds in the NANTEN catalog also means that the shape of the PDF is biased toward high CO intensities; extending MAGMA to fainter clouds would recover a greater fraction of pixels with low CO brightness and narrow the PDFs in Figures 6(c) and (f). Relative to the observed $I$(CO) PDF of the LMC, the M51 $I$(CO) distribution peaks at higher CO intensity, $\langle I(\mathrm{CO})\rangle \sim 12$ K km s$^{-1}$, and is also wider by a factor of $\sim$2 in the logarithm (see Table 1). The difference between the best-fitting LN function derived for the M51 distribution in Figure 6(a) and that in Figure 2(a) is consistent with the differences that we observe for different masking techniques for identifying significant emission within the data cube (see Appendix A).

The PDFs of CO brightness for the three galaxies are presented in the right panels of Figure 6. For M51, we fit the distribution of CO brightness with an LN function with mean $\langle T_{\mathrm{mb}}\rangle = 0.8$ K and logarithmic width $x = 0.4$. This is consistent with the best-fitting LN function derived for the PAWS data in Figure 2(b), which used a more sophisticated masking technique to identify significant emission. Alternatively, a broken power law with a shallow slope of $\sim -1.3$ between $T_{\mathrm{mb}} = 1$ and 4 K and a much steeper slope ($\sim -5.0$) above 4 K also fits the $T_{\mathrm{mb}}$ distribution for M51 reasonably well. For the LMC, the best-fitting LN function has mean $\langle T_{\mathrm{mb}}\rangle = 0.1$ K and logarithmic width $x = 0.3$; there is no sign of a truncation. A simple power law with a slope of $\sim -2.2$ also adequately represents the distribution. There are insufficient pixels with significant emission in the M33 data cube to attempt to fit the $T_{\mathrm{mb}}$ PDF with an LN function. A simple power law with a slope of $\sim -3.6$ provides a reasonable fit to the distribution for pixel values $T_{\mathrm{mb}} \gtrsim 0.3$ K. We note that the slopes of the power laws that fit the $T_{\mathrm{mb}}$ PDFs reproduce the trends observed for the GMC mass distribution in the three galaxies, i.e., a shallow slope for M51 (below $T_{\mathrm{mb}} \sim 4$ K) and a much steeper brightness distribution for the low-mass galaxies (A. Hughes et al., in preparation). We discuss the connection between the shape of the CO PDFs and the GMC mass distribution further in Section 5.2.

## 5. DISCUSSION

### 5.1. Comparison with Previous Observations

Both high resolution and wide-field coverage are necessary to characterize the CO emission in galaxies on spatial scales that are relevant for SF, hence few extragalactic studies have produced PDFs of CO brightness and/or integrated intensity that represent a significant fraction of a galactic disk. One exception is an analysis of the LMC by Wong et al. (2011), which found that the $I$(CO) PDF was roughly consistent on $\sim$10 pc scales, with a narrow LN function ($\langle \Sigma_{\mathrm{H_2}}\rangle = 16\ M_\odot$ pc$^{-2}$, $x \sim 0.3$ dex) at high column densities. The authors noted some evidence for a truncation around $\Sigma_{\mathrm{H_2}} = 200\ M_\odot$ pc$^{-2}$, which they tentatively attributed to opacity effects in the $^{12}$CO($J = 1 \rightarrow 0$) line. Notably, however, the MAGMA data show no evidence for a power-law excess at high column densities, as has been observed on pc scales within star-forming Galactic clouds (e.g., Kainulainen et al. 2009), suggesting that the structure of LMC molecular clouds is still dominated by turbulence on $\sim$10 pc scales.

The CO emission in M51 itself has been analyzed by numerous authors (e.g., Vogel et al. 1988; Rand 1993; Aalto et al. 1999; Helfer et al. 2003; Shetty et al. 2007). With the exception of the recent survey by Koda et al. (2009), however, observations with high spatial resolution have mostly focused on a spiral arm segment (e.g., Schinnerer et al. 2010; Egusa et al. 2011), while studies covering a significant fraction of the disk (e.g., Garcia-Burillo et al. 1993; Schuster et al. 2007) have had a resolution of a few hundred pc or greater, i.e., insufficient resolution to resolve individual GMCs. Rather than examining PDFs, these lower-resolution studies have typically examined radial trends in properties such as the gas velocity dispersion, Toomre's $Q$ parameter, and the molecular gas depletion time $\tau_{\mathrm{H_2}}$ (e.g., Schuster et al. 2007; Hitschfeld et al. 2009). From the PDFs in Section 4.3, we would expect to observe a radial decline in the average value of $\Sigma_{\mathrm{H_2}}$ constructed from azimuthal averages, since the fraction of bright CO emission (as parameterized by the IDI values) decreases along the spiral arms and also because the interarm region occupies an increasing fraction of the disk area with increasing galactocentric radius. Since the mass surface density is an important input for the determination of Toomre's $Q$ and $\tau_{\mathrm{H_2}}$, radial trends in these quantities may likewise reflect a combination of differences between the arm and interarm zones and variations along the spiral arms (an interpretation that would seem to be supported by the map of Toomre's $Q$ presented in Figure 15 of Hitschfeld et al. 2009, for example).

More generally, we note that differences in the basic properties of the CO emission (i.e., peak brightness, velocity dispersion) between the arm and interarm regions of M51 have been reported by several previous studies and often interpreted as evidence for changes in the physical state of the molecular gas as it passes through the spiral arms. While the precise identification of M51's arm and interarm zones varies (usually because M51's gaseous spiral arms appear wider at lower spatial resolution), CO emission in the interarm has been shown to have lower velocity dispersion (e.g., Garcia-Burillo et al. 1993; Aalto et al. 1999; Hitschfeld et al. 2009), lower peak brightness (e.g., Garcia-Burillo et al. 1993; Tosaki et al. 2002), lower SF efficiency (as inferred from the ratio of H $\alpha$ to $^{12}$CO($J = 1 \rightarrow 0$) emission, e.g., Rand 1993; Tosaki et al. 2002), higher $^{12}$CO($J = 1 \rightarrow 0$)/$^{13}$CO($J = 1 \rightarrow 0$) isotopic ratios (e.g., Tosaki et al. 2002), and lower $^{12}$CO($J = 2 \rightarrow 1$)/$^{12}$CO($J = 1 \rightarrow 0$) transitional ratios (e.g., Koda et al. 2012) than emission in the spiral arms. Most of these results suggest that molecular gas in the interarm region has a lower characteristic density than gas within the spiral arms.

Spatial resolution is rarely a limitation for studies of molecular gas in the Milky Way, although previous analyses of Galactic CO emission have tended to focus on the physical properties of GMCs (e.g., Solomon et al. 1987; Roman-Duval et al. 2010), which were quickly recognized to be the preferred—perhaps only—site of high-mass SF in the Galaxy. Recent work has emphasized, however, that faint, spatially extended CO emission contributes significantly to a region's total CO flux (e.g., Goldsmith et al. 2008; Heyer et al. 2009; Liszt et al. 2010). Very recently, Sawada et al. (2012b) presented PDFs of $^{12}$CO($J = 1 \rightarrow 0$) and $^{13}$CO($J = 1 \rightarrow 0$) brightness for an $0.^{\circ}8 \times 0.^{\circ}8$ field toward the Galactic plane at $l \approx 38^{\circ}$, observed using the Nobeyama Radio Observatory (NRO) 45 m telescope. These authors find clear differences between the PDFs constructed from the emission at radial velocities corresponding to the Sagittarius arm and those corresponding to the interarm regions, showing that the structural properties of the molecular gas vary in response to Galactic structure. They conclude that compact, high-brightness CO structures develop downstream of the molecular spiral arms, where they are spatially coincident with signatures of active SF (e.g., H II regions). Sawada et al. (2012b) point out

that their result is a rediscovery of a conclusion that had already been drawn by earlier studies. Sanders et al. (1985), for example, observed a connection between the location of Galactic molecular clouds in longitude–velocity space and their peak brightness temperature: "hot" (i.e., high-brightness) clouds were preferentially located in the spiral arms traced by H II regions (Georgelin & Georgelin 1976). Egusa et al. (2011) present a qualitatively similar scenario for a ∼2 kpc segment of M51's inner spiral arm, showing that both high-mass ($\sim 10^6\ M_\odot$) CO clumps and H II regions are preferentially located downstream of the spiral arm ridge line (note, however, that the high-brightness CO structures described by Sawada et al. (2012b) occur on much smaller spatial scales than the structures observed by Egusa et al. (2011) in M51).

Although the spatial resolution of the PAWS data is considerably worse than that of Galactic surveys, the PDFs in Figure 5 show similar trends as those reported by Sawada et al. (2012b). As we noted in Section 4.3, the PDFs of the interarm region resemble narrow LN functions, while the PDFs in the central and spiral arm regions reach higher maximum intensities and tend to be better represented by broken power laws. These variations in shape are reflected by the BDI and IDI values: low-brightness emission dominates the total flux in both the arm and interarm environments, but the relative contribution from bright emission increases in the spiral arms. Bright emission is most dominant in the center of M51, where ∼25% of the total CO flux arises from pixels with $T_{\rm mb} > 4$ K (in comparison, less than 5% of the emission in the interarm region is brighter than 4 K). Similar to Sawada et al. (2012b), we find that the BDI and IDI values are higher on the downstream side of the spiral arms than on the upstream side. Tracers of high-mass SF, e.g., H$\alpha$, 24 $\mu$m, and far-ultraviolet emission, also appear to be preferentially located downstream of arms (Schinnerer et al. 2013), again consistent with the Galactic results. We discuss the connection between SF and the shape of the CO PDFs for different M51 environments in more detail in Section 5.3.

The fact that a similar relationship between CO emission properties and spiral arm structure is observed in both M51 and the Milky Way would seem to support the argument by Sawada et al. (2012b) and Sawada et al. (2012a) that the arm–interarm variations they observe reflect genuine changes in the density distribution of the Galactic CO-emitting gas. One important caveat, however, is that the PAWS data have much lower spatial resolution (∼40 pc) than the Galactic NRO data ($\lesssim$1 pc). In particular, the lower CO brightness temperatures that we observe in M51 ($T_{\rm mb} \lesssim 16$ K) indicate that our PAWS measurements reflect a combination of the average kinetic temperature and the filling factor of the CO-emitting gas within a resolution element. Variations in CO brightness on $\lesssim$1 pc scales, in contrast, should mostly track variations in gas temperature and/or density since beam dilution should be minimal on these scales. Some of the variation between high and low BDI values in M51 will reflect changes in the covering fraction of the CO emission for the different M51 environments, as well as differences in the intrinsic brightness temperature of the CO-emitting structures that are more directly comparable with the variations described by Sawada et al. (2012b).

### 5.2. Comparison with GMC Properties

In Section 4.3, we described variations in the characteristic shape of the CO PDFs for different M51 environments. To what extent are these differences manifested in variations of the properties of GMCs within each environment or of the ensemble

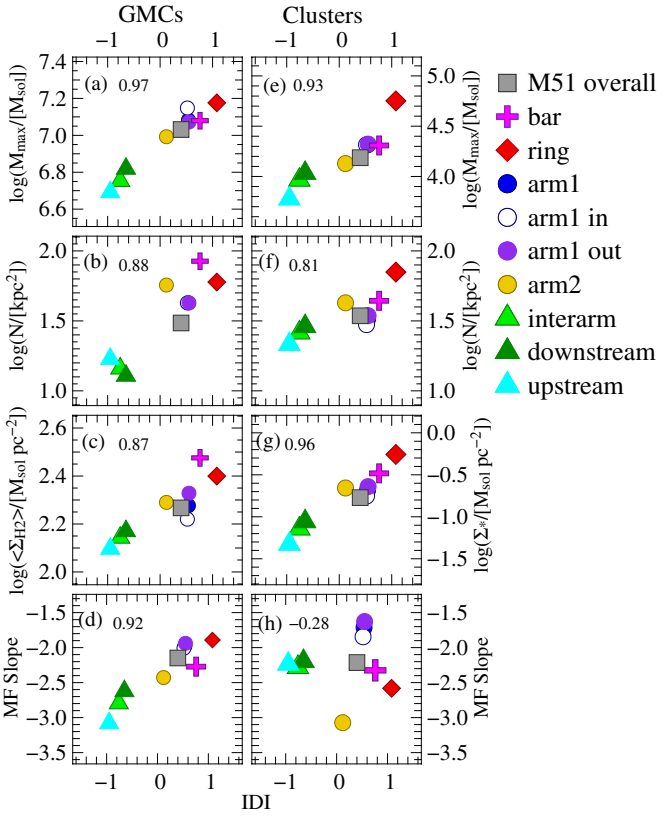


**Figure 7.** Properties of the GMC (left column) and young (<10 Myr) stellar cluster (right column) populations in different M51 environments compared with the shape of the CO PDFs. The Spearman rank correlation is indicated at the top left of each panel.

properties of a GMC population (e.g., its mass distribution)? Intuitively, we would expect some connection between GMCs and the presence of high-brightness CO emission, since most methods for identifying GMCs from CO data cubes invoke either a brightness threshold or local maximum in the CO brightness distribution in order to define cloud structure. The connection may be rather indirect, however, since the fraction of CO emission above the PAWS sensitivity limit that is associated with the observationally defined GMCs varies between 40% and 65%, depending on galactic environment (Colombo et al. 2013a).

We examined the relationship between GMC properties and the shape of the CO PDFs using the cloud catalog presented by Colombo et al. (2013a) and the BDI and IDI values calculated in Section 4.3. Since the BDI and IDI values themselves exhibit a tight one-to-one correlation, for simplicity we refer only to the IDI values in the following sections. We illustrate some of these correlations in the left column of Figure 7. Environments where bright CO emission is more dominant (i.e., with more positive IDI values) are associated with a higher maximum GMC mass $M_{\rm gmc,95}$, which we estimate using the 95th percentile of the GMC virial mass distribution (panel (a)), a greater number surface density of GMCs $\mathcal{N}_{\rm gmc}$ (panel (b)), and a higher average surface density for individual GMCs $\langle\Sigma_{\rm H_2}\rangle$ (panel (c)). The IDI is also strongly correlated with the slope of the GMC mass spectrum $\gamma_{\rm gmc}$: in environments with more bright emission, the mass spectrum is shallower (panel (d)). For observations with low resolution (i.e., where a single resolution element is much larger than the characteristic size of a GMC), a good correlation between the prevalence of bright

CO emission and the mass and mass surface density of identified cloud structures might arise simply due to higher filling factors of CO emission, i.e., increases in the measured CO-integrated intensity reflect a greater number of CO-emitting clouds within the telescope beam, rather than changes in the intrinsic properties of GMCs. We do not consider this to be the cause of the good correlations in Figure 7, however, since the PAWS resolution (∼40 pc) is well matched with the characteristic size of an individual Galactic GMC (50 pc, e.g., Blitz 1993) and considerably less than the typical spacing between the identified GMCs (a few times hundred pc or greater; Colombo et al. 2013a). The peak CO brightness temperatures of the GMCs range from ∼2 to 16 K, which is comparable with the values observed for Galactic GMCs (5–10 K; Solomon et al. 1987). Since the molecular gas in M51 GMCs appears to have a similar kinetic temperature as in Galactic GMCs (∼10 K; Schinnerer et al. 2010), this again suggests that the filling factor of the CO emission in M51 GMCs is close to unity.

It is remarkable that the GMC properties are often more strongly correlated with the shape of the CO PDFs than other quantities with which they might also be expected to correlate. In particular, we note that $M_{\rm gmc,95}$ and $\gamma_{\rm gmc}$ are more tightly correlated with the IDI than with the total CO luminosity or the total number of GMCs in each region (the latter plots are not shown). This would seem to confirm that an increase in the maximum GMC mass is not simply due to an increase in the available gas reservoir and more adequate sampling of the top end of the GMC mass function (i.e., a sample size effect) and that the good correlation among the IDI, $M_{\rm gmc,95}$, and $\gamma_{\rm gmc}$ arises because the density distribution of the molecular ISM plays a role in regulating the GMC mass distribution. It is also noteworthy that the IDI increases with both the number density of GMCs $\mathcal{N}_{\rm gmc}$ *and* the average surface density of the individual clouds $\langle\Sigma_{\rm H_2}\rangle$. This suggests that a distinction that is sometimes drawn by empirical studies of extragalactic SF between an increase in the number of GMCs per resolution element and variations in the $H_2$ surface density on the scale of individual clouds (e.g., Bigiel et al. 2008) is somewhat artificial: at least in the inner disk of M51, clouds in environments with more GMCs per unit area also tend to have higher average surface densities.

The good correlation between the IDI and $\gamma_{\rm gmc}$ in panel (d) of Figure 7 is especially noteworthy. Considerable theoretical and observational effort has been devoted to showing how the shape of the stellar initial mass function might be inherited from the density structure of interstellar gas (e.g., Hopkins 2012; Chabrier & Hennebelle 2010 and references therein), with many studies adopting the shape of the GMC mass function as a description of the latter. A major problem with using GMC mass spectra for this purpose, however, is that the decomposition algorithm has a major impact on the identification and parameterization of cloud structures and hence the shape of the resulting mass distribution (e.g., Wong et al. 2011; Reid et al. 2010). Moreover, many widely used decomposition methods are not flux conservative, discarding a considerable fraction of the CO emission that is unambiguously detected within a spectral line data cube. As a description of how dense gas is distributed within galaxies, PDFs avoid these ambiguities even though, as we show in Appendix B, the resolution of the observational data must be well matched to the physical scales of interest in order to accurately capture the shape of the PDF. The PDF also conveys no information about the characteristic size of dense gas structures, moreover, so a more complete description of the organization of the dense ISM strictly requires an analysis of the CO PDF in conjunction with a metric such as the spatial power spectrum (as suggested by, e.g., Bournaud et al. 2010). Nonetheless, the plots in the left column of Figure 7 indicate that there is a strong relationship between the shape of the PDF and the mass distribution and properties of GMCs within M51 environments, suggesting that in real galactic disks the presence of bright emission and the development of massive molecular structures are physically linked. Testing whether a similar connection between the GMC mass function and shape of the PDF holds across a range of galaxy types is a project that should become feasible once ALMA acquires cloud-scale imaging of CO emission across the full galactic disk for a large sample of nearby galaxies.

### 5.3. Comparison with Properties of Stellar Clusters

Another motivation for constructing the CO PDFs across a range of M51 environments is to assess whether there are connections among empirical tracers of SF activity and the density distribution of molecular gas. Several empirical calibrations for the SF rate exist in the literature (for a detailed comparison of the limitations and assumptions of different methods, see Leroy et al. 2012), but here we restrict our analysis to comparing the shape of the CO PDFs with the properties of young stellar clusters identified by Chandar et al. (2011) using multi-color images of M51 obtained by the Advanced Camera for Surveys onboard the *Hubble Space Telescope* (Mutchler et al. 2005). The interested reader is referred to Chandar et al. (2011) for a description of the methods used to select clusters and to derive physical quantities such as their age and mass. The relationship between CO emission and other SF tracers within the PAWS field is discussed in several companion papers (Meidt et al. 2013; Schinnerer et al. 2013).

As for GMCs, we find evidence for a strong connection between the prevalence of bright CO emission and M51's young ($\tau \leqslant 10^7$ Myr) cluster population. In particular, more positive IDI values are associated with a higher maximum young cluster mass $M_{\rm yc,95}$ (defined analogously to $M_{\rm gmc,95}$) and with a higher number surface density $\mathcal{N}_{\rm yc}$ and combined mass surface density $\mathcal{M}_{\rm yc}$ of young clusters (Figures 7(e)–(g)). The origin of these trends would seem to lie in a physical—as opposed to statistical—connection between young clusters and GMCs: $M_{\rm yc,95}$, $\mathcal{N}_{\rm yc}$, and $\mathcal{M}_{\rm yc}$ are better correlated with the average GMC mass surface density ($\langle\Sigma_{\rm H_2}\rangle$) and maximum GMC mass ($M_{\rm gmc,95}$) than with the total number of young clusters or GMCs within each M51 environment.

An exception to the good correspondence between the shape of the CO PDFs and the properties of GMCs and young stellar clusters is the slope of the cluster mass distribution: while there is a clear trend for the GMC mass spectrum to become shallower in regions where bright CO emission is more prevalent, a connection between the slope of the young cluster mass function and the shape of the CO PDFs is less obvious (see panels (d) and (h) of Figure 7). There is some indication that the mass distribution of the young cluster populations in the arm and interarm regions follows the same trend with IDI as GMCs, but within the central kpc of M51 (i.e., the molecular ring and nuclear bar regions) the young cluster mass distributions are steep ($\lesssim -2.5$) even though bright CO emission is relatively dominant there.

In Figure 8, we plot the slope of the young cluster mass spectrum directly against the slope of the GMC mass spectrum for the different M51 environments. Various techniques for

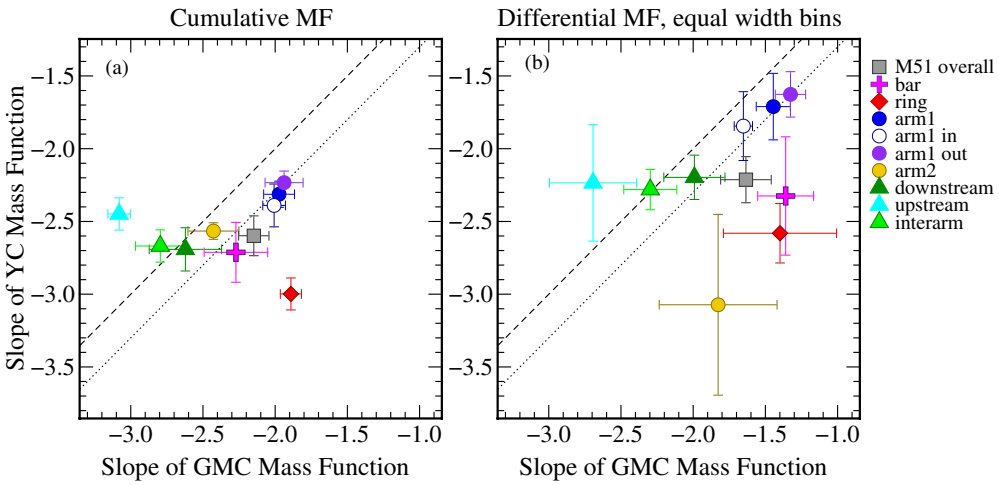


**Figure 8.** Slope of the young cluster mass function versus the GMC mass function for different dynamical environments within M51. Panel (a) shows the results using a cumulative formulation for the mass distribution; panel (b) shows the results for a differential representation. In both panels, the error bars reflect the dispersion in the estimated slopes (see Appendix C). The dashed diagonal line indicates equality and the dotted diagonal line represents $\gamma_{\rm gmc} = \gamma_{\rm yc} + 0.3$. The plot annotations are the same as in Figure 7.

estimating the slope of the mass spectrum have been used by empirical studies of young clusters and GMCs (e.g., differential versus cumulative mass distributions, bins of equal width versus bins containing an equal number of objects) and the derived slope is known to be sensitive to factors such as cloud decomposition algorithm, the adopted low-mass completeness limit, and undersampling and/or the existence of a physical truncation to the distribution at high masses. We constructed both differential and cumulative mass distributions for the GMC and young cluster populations and, for each variant, we estimated the slope multiple times using different binning strategies (in the case of the differential mass distributions) and mass ranges to calculate the fit. We describe these tests more fully in Appendix C. The two panels of Figure 8 show the results using a cumulative representation (panel (a)) and a differential representation (panel (b)) for the mass distributions. In both panels, the error bars reflect the dispersion in the estimated slopes of the GMC and young cluster mass spectra in each environment. Despite the systematic uncertainties that limit the accuracy of any individual measurement of the mass distribution slope, we can therefore confidently draw two conclusions from Figure 8. The first is that while there is reasonable agreement between $\gamma_{\rm gmc}$ and $\gamma_{\rm yc}$ for the arm and interarm environments of M51, the slope of the mass distribution is not universal, i.e., the same values of $\gamma_{\rm gmc}$ and $\gamma_{\rm yc}$ do not hold everywhere within M51. Second, agreement between the slopes of the GMC and young cluster mass distributions is not ubiquitous. When averaged across the entire PAWS field and for some of the arm and interarm regions, $\gamma_{\rm gmc}$ and $\gamma_{\rm yc}$ agree to within ∼0.3 dex, but for the molecular ring and upstream environments $\gamma_{\rm gmc} \not\approx \gamma_{\rm yc}$, regardless of the method used to represent the mass functions.

The trends in Figure 8 are remarkable since the observed similarity between $\gamma_{\rm gmc} \approx -1.7$ and $\gamma_{\rm yc} \approx -2.0$ is frequently cited as evidence for the weak mass dependence of both the efficiency of SF in GMCs and probability of cluster disruption. In their investigation of stellar feedback and disruption of GMCs, for example, Fall et al. (2010) derive relations between $\gamma_{\rm gmc}$ and $\gamma_{\rm yc}$, which for isolated, bound systems in the absence of magnetic support are linked via the slope of the mass versus size relationship of GMCs. Fall et al. (2010) examine the limiting regimes of energy- and momentum-driven feedback, arguing that the constant surface density of GMCs ($M \propto R^2$) ensures that $\gamma_{\rm gmc} \sim \gamma_{\rm yc}$ regardless of the type of feedback that dominates GMC disruption.

In a globally averaged sense, the young cluster and GMC populations of M51 would seem to conform to the model outlined by Fall et al. (2010). In this case, $\gamma_{\rm gmc} = -1.7$, $\gamma_{\rm yc} = -2.1$, and, for momentum-driven feedback, the predicted slope of the GMC mass-size relation is $\alpha = 1.8$, in acceptable agreement with the observed value ($\alpha_{\rm obs} = 2.1$; Colombo et al. 2013a). However, our results for individual environments within M51 suggest a more nuanced interplay among molecular gas, young clusters, and galactic structure. Downstream of the spiral arms, for example, $\gamma_{\rm gmc} \sim \gamma_{\rm yc} \approx -2.0$ and $\alpha_{\rm obs} = 1.8$, in good agreement with the model prediction for energy-driven feedback. Yet upstream of the spiral arms (where $\gamma_{\rm gmc} \sim \gamma_{\rm yc} \approx -3.0$), in the molecular ring ($\gamma_{\rm gmc} \approx -1.4$, $\gamma_{\rm yc} \approx -2.7$) and in the first spiral arm pattern of M51 ($\gamma_{\rm gmc} \approx -1.5$, $\gamma_{\rm yc} \approx -2.1$), the exponent of the mass–size relationship predicted by Fall et al. (2010) is too shallow compared with the observed value of 0.4–1.0 dex, regardless of the assumed feedback mechanism. This suggests that there may be regions within galactic disks where physical processes that would seem to be excluded by Fall et al. (2010), e.g., cluster coalescence, mass-dependent cluster/GMC disruption, or a dominant role for energy-driven feedback, are in fact important. More generally, however, it highlights how valuable information can be lost in the calculation of galaxy-wide averages. With data sets that yield statistically significant samples of GMCs and other star-forming phenomena within ∼kpc-scale regions, it is timely that physical quantities (for example, based on a consideration of galaxy dynamics and/or ISM properties) determine the environments where GMC properties and extragalactic SF are investigated, rather than relying solely on radial profiles and/or apertures that are "blind" to their location with respect to galactic structure.

### 5.4. Comparison with Numerical Simulations of Galactic Disks

Our analysis in this paper was prompted, in part, by numerical simulations showing that the gas density distribution in galactic disks is well represented by a single LN function spanning several orders of magnitude (e.g., Wada & Norman 2007). If this is an accurate description of real galactic disks, then the result offers insight into the origin of the KS law, which can be

reproduced from a LN density PDF with a limited number of plausible assumptions, such as a critical density threshold for SF (Elmegreen 2002) or a direct proportionality between the local gas and SF rate densities (e.g., Kravtsov 2003). While the overall $I$(CO) and $T_{\rm mb}$ PDFs for the PAWS field are roughly LN, our results in Section 4.3 show that this average PDF shape obscures considerable diversity among the PDFs observed for different ∼kpc-sized regions within M51. Since the regions that we use to investigate the PDFs are defined according to dynamical criteria, our basic result is that large-scale dynamical processes in M51's inner disk have an observable effect on the density (and column density) distribution of M51's molecular ISM.

There are several further characteristics of our observed CO PDFs that are noteworthy in relation to the simulation results. For example, Wada & Norman (2007) find an increase in the logarithmic width of the PDF of ∼0.3 dex for an order of magnitude increase in the mean gas density. This is roughly consistent with the variation in the width of the $I$(CO) PDFs of M51 and the LMC, between which the average $H_2$ column density also varies by a factor of ∼10 (see Section 4.4). However, we caution that several effects limit the extent to which we can compare our observed CO PDFs with the density PDFs from simulations. The first is that the simulations describe gas density across six orders of magnitude, corresponding not only to the molecular ISM but also to the atomic and warm ionized phases. In practical terms, this makes the numerical result difficult to verify, since different observational tracers must be used to probe different phases of the interstellar gas and each of them are sensitive to a much narrower range of densities (and column densities) than the full dynamic range of the simulated PDFs.

The few simulations that include explicit treatment of molecular chemistry tend to find a range of densities between ∼1 and $10^3$ cm$^{-3}$ for the $H_2$ gas in galactic disks and that the distribution exhibits a sharp cut-off below the $H_2$ self-shielding limit ($n \lesssim 5$ cm$^{-3}$; see, e.g., Figure 11 of Dobbs et al. 2008). The use of $^{12}$CO($J = 1 \rightarrow 0$) emission to trace the $H_2$ column density should narrow the observed PDF even further, since at moderately low extinction ($A_{\rm V} \sim 1$ mag, e.g., Wolfire et al. 2010) $H_2$ can self-shield while CO molecules are photodissociated. At high $H_2$ column densities ($N(H_2) \gtrsim 10^{22}$ cm$^{-2}$), on the other hand, the CO-emitting structures within a GMC will start to overlap and shadow each other, leading to a saturation of $I$(CO) intensities (e.g., Shetty et al. 2011). Feldmann et al. (2012) show that this saturation should occur at $I$(CO) intensities near a few 100 K km s$^{-1}$. In general, however, the $I$(CO) PDFs in Figure 4 show no evidence for a peak at these intensities caused by a "pile-up" of saturated pixels, but instead more closely resemble their pure $N(H_2)$ PDFs after they exclude pixels with low CO-integrated intensities (<0.2 K km s$^{-1}$; see Figure 8 of Feldmann et al. 2012). We suggest that this is because the typical CO linewidths in M51 are much larger than the two possibilities considered by Feldmann et al. (2012; i.e., a constant linewidth of 3 km s$^{-1}$or a virial scaling of the linewidth with mass surface density). As a consequence, the majority of the CO-emitting molecular structures in M51 do not shadow each other in velocity space and hence $I$(CO) remains a relatively good tracer of the $H_2$ column density. This is consistent with recent studies of gas and dust in M51, which suggest that the $X_{\rm CO}$ factor has a roughly Galactic value throughout the disk (e.g., Schinnerer et al. 2010; Tan et al. 2011; Mentuch Cooper et al. 2012).

What insights can models provide regarding the diversity of distribution shapes that we observe? As noted in the Introduction, the PDF for supersonically turbulent isothermal gas is LN when the influence of gravity is negligible. In this case, the logarithmic width of the PDF $x$ varies with the Mach number $\mathcal{M}$ according to $x^2 \approx \ln(1 + 0.25\mathcal{M}^2)$ (Padoan et al. 1997). Across a galactic disk, however, the temperature and average density of the molecular gas will vary with location. Thus, a more realistic expectation for the observed density PDF on global to kpc scales may be the convolution of the local LN PDF (reflecting the distribution of densities within a region over which the average gas density $\rho_{\rm ave}$ and Mach number are relatively constant) with the PDFs of $\rho_{\rm ave}$ and $\mathcal{M}$ within the galactic disk. Elmegreen (2011) recently considered such a model, presenting convolution PDFs for several idealized cases of gas clouds with different radial density profiles and variable Mach numbers (see his Figure 1). The resulting PDFs clearly diverge from a pure LN shape. As clouds become more centrally condensed (and hence more dominated by self-gravity), the convolution PDFs develop a power-law tail at high densities, with a slope that varies inversely with the slope of the density profile. If the Mach number decreases at higher average densities, on the other hand, the convolution PDF appears truncated relative to a pure LN since the local PDFs get narrower with increasing $\rho_{\rm ave}$.

In broad terms, the analysis by Elmegreen (2011) suggests that the diverse shapes of the $I$(CO) PDFs in Figure 4 reflect large-scale variations in the average density, temperature, and/or velocity fluctuations for the molecular gas within different M51 environments. In reality, these properties are likely to vary simultaneously, so attributing a specific PDF morphology to a variation in one physical quantity and/or process is not straightforward. Nevertheless, it is suggestive that the $I$(CO) PDFs in the interarm region—where we might expect the temperature, density, and velocity structure of the molecular gas to be determined by cloud-scale processes—resemble the pure LN shapes expected for isothermal supersonically turbulent molecular gas, whereas the $I$(CO) PDFs in M51's spiral arms—where the molecular gas not only reaches higher densities, but its velocity structure can be influenced by large-scale dynamical effects such as streaming motions and the spiral shock—more obviously diverge from a LN shape. The molecular ring region, where the $I$(CO) PDF is very broad and almost flat-topped, is arguably the extreme case both in terms of dynamical effects and SF activity. Although shear and large-scale non-circular motions should be low in the ring, the molecular gas accumulates here due to opposing bar and spiral torques and the average gas velocity dispersion is relatively high (Colombo et al. 2013a). The level of SF activity in the ring is also high (Schinnerer et al. 2013), so feedback from nascent stars may also have a strong effect on the distribution of gas densities in this region.

Finally, we note that Hopkins et al. (2012) have recently shown that the dominant mode of stellar feedback (and not just the total amount of SF) has an observable effect on the shape of the density PDF for the cold gas component in their simulated galaxies. Like Wada & Norman (2007), they find that the width of the density PDF decreases for systems with lower average gas densities. The density PDFs of their simulated gas disks show striking departures from lognormality (see their Figures 10 and 11), however, which they attribute to the inclusion of cooling, self-gravity, and a physically motivated implementation of different feedback mechanisms in their simulations. In particular, they find that radiation pressure is crucial for suppressing a pile-up of gas with high densities ($n \gtrsim 10^4$ cm$^{-3}$), since pure gas heating (e.g., by supernovae, stellar winds, and H II photoionization) is

ineffective in disrupting dense gas clumps where the cooling time is much shorter than the dynamical time. While the overall shapes of the $I$(CO) and $T_{\rm mb}$ PDFs for different M51 environments almost certainly reflect the combined action of several distinct physical processes, the absence of a secondary peak in the PDFs at high CO intensities would seem to confirm that the dominant feedback mechanism in M51 must be effective at preventing the build-up of high-density material.

## 6. CONCLUSIONS

In this paper, we have presented the PDFs of CO-integrated intensity and CO brightness within the inner disk of M51, using new high-resolution (∼40 pc) data from the PdBI Arcsecond Whirlpool Survey (PAWS; Schinnerer et al. 2013). We have compared the PDFs of these properties for different environments within the PAWS field and we have compared PDFs constructed using high-resolution CO data sets for two nearby dwarf galaxies. We report the following results and conclusions.

1. On ∼40 pc scales, the distribution of $I$(CO)-integrated intensities within the inner ∼11 × 7 kpc of M51 spans ∼1.5 orders of magnitude above the 3$\sigma$ sensitivity limit of the PAWS data. The shape of the $I$(CO) PDF is consistent with a LN function with a mean of 20 K km s$^{-1}$ and a logarithmic width of 0.4. Relative to this LN function, there is some evidence that the observed PDF is truncated for $I$(CO) values greater than ∼200 K km s$^{-1}$.
2. The CO brightness temperatures that we measure for the inner disk of M51 span ∼1 to 10 K, where the lower limit corresponds to our survey's 3$\sigma$ sensitivity limit. The shape of the $T_{\rm mb}$ PDF can be represented by a LN function with a mean of 0.9 K and a logarithmic width of 0.3, but a broken power law with a slope of ∼−1.4 for $1 < T_{\rm mb} < 5$ K and a much steeper slope of ∼−4.9 for $T_{\rm mb} > 5$ K is an equally adequate description of the distribution.
3. The CO PDFs that describe the emission in the inner disk of M51 are clearly different from the PDFs obtained for M33 and the LMC. The maximum $I$(CO) and $T_{\rm mb}$ values observed in M51 are 1–1.5 dex higher than in the two low-mass galaxies. The CO PDFs in M51 are also wider, consistent with numerical results indicating that the width of the density and column density PDF increases with the average gas density of a galactic disk (e.g., Wada & Norman 2007).
4. The CO PDFs for different dynamical environments within M51's inner disk exhibit diverse shapes. The CO PDFs in the interarm regions are narrower than in the spiral arms, nuclear bar, and molecular ring regions. The distributions of $I$(CO) and $T_{\rm mb}$ are approximately LN in the interarm, while the PDFs in the arms, ring, and bar exhibit strong departures from lognormality such as power-law slopes and/or truncations at high CO intensities. While a LN function may provide an adequate description for the overall gas distribution within a galaxy, phenomena such as streaming motions, spiral arm shocks, and SF feedback produce observable changes to the gas density distribution on kpc scales within galaxies.
5. To avoid assuming a particular functional form for the CO PDFs in M51, we characterized their shape using the brightness (or integrated intensity) distribution index, originally devised by Sawada et al. (2012b), a simple parameter that specifies the ratio between bright and faint emission. With this, we showed that the shape of the CO PDFs for dynamically defined, kpc-scale environments within M51 are strongly correlated with physical properties of the GMC and young stellar cluster populations of those environments. We also infer their SF activity. The implications of this result for interpreting the observational scatter in extragalactic SF laws are explored in several companion papers (Meidt et al. 2013; Schinnerer et al. 2013; S. Pardy et al., in preparation).
6. Consistent with the predictions from numerical simulations (e.g., Wada & Norman 2007), we find a shallow increase in the width of the PDF with increasing average gas surface density. The dynamic range of the observed $I$(CO) PDFs is also in approximate agreement with the distributions of $H_2$ column density obtained by simulations that include an explicit treatment of molecular chemistry (e.g., Dobbs et al. 2008; Feldmann et al. 2012), but we do not observe a secondary peak in the PDFs at high CO intensities corresponding to CO saturation. We suggest that this is because the CO linewidths in M51 are typically larger than the linewidths adopted by the simulations, so the "mist-model" explanation (Dickman et al. 1986) of the Galactic $X_{\rm CO}$ factor remains valid even at high $H_2$ column densities.
7. We show that the diverse shapes of the CO PDFs in M51 are qualitatively similar to the deviations from lognormality expected from the combined action of SF feedback and large-scale variations in density, temperature, and velocity structure throughout M51's inner disk. Our results suggest that SF feedback on small scales and dynamical effects on large scales (e.g., the influence of the stellar bar and spiral density way) together regulate the velocity structure of the molecular gas and that these processes in combination with gas self-gravity determine the shape of the CO PDFs. Isolating the dominant physical process responsible for the morphology of each PDF will require a more detailed comparative analysis with theoretical models, however.
8. The precise shape of the $I$(CO) and $T_{\rm mb}$ PDFs is sensitive to several non-physical effects including resolution, sensitivity, and the method used to identify significant emission within a spectral line cube. These caveats should be kept in mind by future studies that compare the PDFs derived from CO observations of different galaxies or aim to validate numerical models using observational results. In particular, we note that the estimated logarithmic width of the PDFs tends to decrease for data sets with poorer sensitivity and that degrading the observational resolution to a spatial scale greater than the characteristic spacing between high-brightness structures can produce the appearance of a threshold in the PDFs. This result is not unique to PDFs of CO emission and suggests that observations of thresholds on kpc scales should be interpreted with care.

We thank R. Chandar for providing the catalog of M51 stellar clusters. We thank the IRAM staff for their support during the observations with the Plateau de Bure Interferometer and the 30 m telescope. D.C. and A.H. acknowledge funding from the Deutsche Forschungsgemeinschaft (DFG) via grant SCHI 536/5-1 and SCHI 536/7-1 as part of the priority program SPP 1573 "ISM-SPP: Physics of the Interstellar Medium." C.L.D. acknowledges funding from the European Research Council for the FP7 ERC starting grant project LOCALSTAR. T.A.T. acknowledges support from NASA grant No. NNX10AD01G. During this work, J.P. was partially funded by the grant ANR-09-BLAN-0231-01 from the French *Agence*

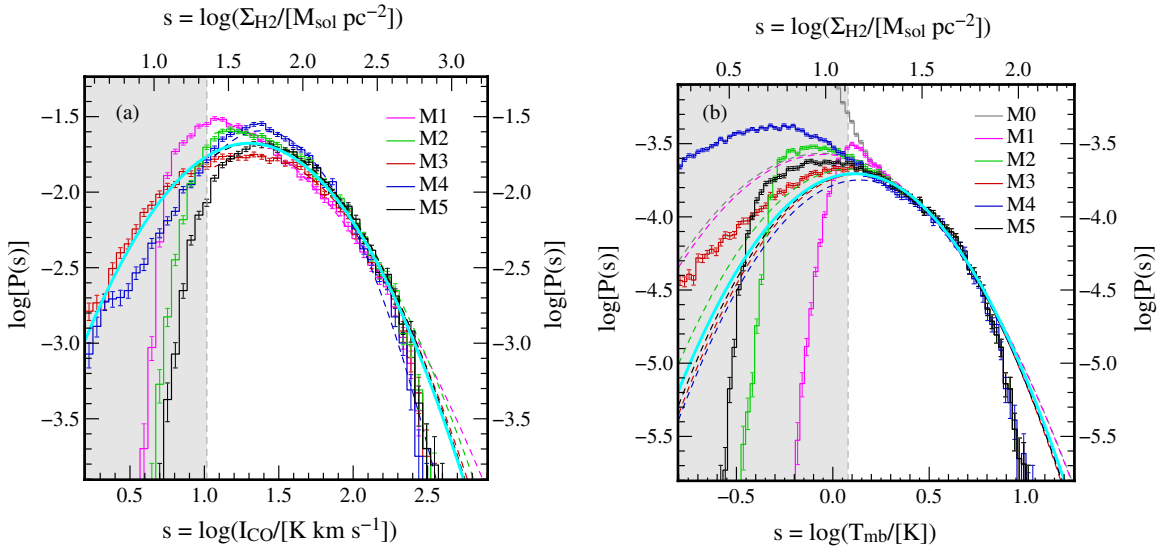


**Figure 9.** PDFs of (a) $I$(CO) and (b) $T_{\rm mb}$ for the PAWS field. The different colors represent PDFs obtained from different masking techniques to identify significant emission within the data cube (see the text). The dashed parabola indicates the LN function that provides the best fit to the corresponding PDF. The thick cyan line in panel (a) represents an LN function with mean $\langle I(\mathrm{CO})\rangle = 20$ K km s$^{-1}$ and logarithmic width $x = 0.45$; in panel (b), the cyan line represents an LN function with mean $\langle T_{\rm mb}\rangle = 1.3$ K and logarithmic width $x = 0.35$. In both panels, the gray shaded region indicates values beneath the nominal $3\sigma_{\rm rms}$ sensitivity limit. The top horizontal axis indicates the equivalent $H_2$ surface density for the $I$(CO) or $T_{\rm mb}$ value on the lower axis, assuming $X_{\rm CO} = 2 \times 10^{20}$ cm$^{-2}$ (K km s$^{-1}$)$^{-1}$ and a helium contribution of 1.36 by mass. The error bars represent the uncertainty associated with simple counting ($\sqrt{N}$) errors.

*Nationale de la Recherche* as part of the SCHISM project (http://schism.ens.fr/). E.S., A.H., and D.C. thank the NRAO for their support and hospitality during their visits in Charlottesville. E.S. thanks the Aspen Center for Physics and the NSF grant No. 1066293 for hospitality during the development and writing of this paper. S.G.B. acknowledges economic support from Junta de Andalucia grant P08 TIC 03531. The National Radio Astronomy Observatory is a facility of the National Science Foundation operated under cooperative agreement by Associated Universities, Inc.

## APPENDIX A

## MASKING METHODS

As discussed by Pety et al. (2013), a number of different techniques for constructing CO-integrated intensity images have been presented in the literature (e.g., Helfer et al. 2003; Dame 2011; Wong et al. 2011). These include the following.

1. A *sigma-clipping* method, M1, whereby pixels containing emission below $n\sigma_{\rm rms}$ are blanked. $\sigma_{\rm rms}$ is the rms of the noise variations, which we calculate for each independent line of sight. For the comparison in this Appendix, we adopted $n = 3$.
2. A *dilated mask* method, M2, which identifies islands of significant emission by selecting peaks above a threshold of $t\sigma_{\rm rms}$ across two contiguous velocity channels. The preliminary mask is then expanded to include all contiguous pixels with emission above $e\sigma_{\rm rms}$. We adopted $(t, e) = (5, 1.2)$.
3. A *smooth-and-mask* method, M3, which generates a version of the cube that has been spatially smoothed to an angular resolution of $\theta$ and identifies emission in the smoothed cube above a significance threshold $m\sigma_{\rm rms}$. The blanking mask is then transferred back to the original (i.e., full resolution) data cube. We adopted $(\theta, m) = (3\farcs6, 5)$.
4. An *H I velocity prior* method, M4, which assumes that all of a galaxy's CO emission arises in velocity channels within a restricted interval, $\Delta V$, around the radial velocity corresponding to the peak of the H I line profile for each line of sight. We used $\Delta V = 50$ km s$^{-1}$.

In addition to these, we defined a final mask for the PAWS cube that optimized flux recovery while eliminating anomalous features in the map of M51's velocity field (M5). The construction of this mask is described in detail by Colombo et al. (2013a). Example $I$(CO) maps for the PAWS field constructed using each of the five techniques are shown in Figure 23 of Pety et al. (2013).

In Figure 9(a), we show the PDFs obtained from the different $I$(CO) maps. It is clear that the map construction method affects the shape of the $I$(CO) PDF. Differences between the curves are apparent up to ∼60 K km s$^{-1}$, which is considerably greater than our nominal $5\sigma_{\rm rms}$ sensitivity limit (∼18 K km s$^{-1}$). The mean ($s_0$) and logarithmic width ($x$) of the best-fitting LN function to each PDF in Figure 9(a) are listed in Table 3. The PDF from the $I$(CO) map constructed using the dilated mask (M2) is the most similar to the PDF from our preferred mask (M5), although it recovers fewer pixels than M5 with $10 < I(\mathrm{CO}) < 60$ K km s$^{-1}$. The same applies to the PDF corresponding to the H I velocity prior method (M4), although this PDF also slightly underestimates the number of high-intensity pixels ($I(\mathrm{CO}) \gtrsim 160$ K km s$^{-1}$). Inspection of the CO velocity dispersion map for the PAWS field shows that there is a small fraction of pixels with FWHM linewidths greater than 17 km s$^{-1}$ (mostly in the nuclear bar and southern spiral arm regions), so our chosen velocity interval of 50 km s$^{-1}$ excludes some genuine emission in the wings of these line profiles. The smooth-and-mask technique (M3) recovers the least emission at intermediate $I$(CO) values. This is because we used a relatively large smoothing kernel and a high-significance threshold, so compact regions with moderate significance in the original data cube are excluded from the final map. The large smoothing kernel is also the reason why the M3 map does not show a sharp cut-off at a low $I$(CO) value, as it incorporates many pixels with low significance that are adjacent to high-brightness

**Table 3**
Fit Parameters for CO PDFs in Figures 9 and 12

| Figure | CO Property | Description | Mean $s_0$ | Logarithmic Width $x$ | Goodness of Fit $\epsilon$ |
|---|---|---|---|---|---|
| 9(a) | $I$(CO) | M1 | 6.3 K km s$^{-1}$ | 0.62 | 0.10 |
| 9(a) | $I$(CO) | M2 | 15.3 K km s$^{-1}$ | 0.50 | 0.08 |
| 9(a) | $I$(CO) | M3 | 21.8 K km s$^{-1}$ | 0.45 | 0.07 |
| 9(a) | $I$(CO) | M4 | 24.4 K km s$^{-1}$ | 0.36 | 0.05 |
| 9(b) | $T_{\rm mb}$ | M0 | 0.9 K | 0.40 | 0.19 |
| 9(b) | $T_{\rm mb}$ | M1 | 0.9 K | 0.40 | 0.18 |
| 9(b) | $T_{\rm mb}$ | M2 | 1.2 K | 0.36 | 0.20 |
| 9(b) | $T_{\rm mb}$ | M3 | 1.4 K | 0.34 | 0.19 |
| 9(b) | $T_{\rm mb}$ | M4 | 1.4 K | 0.34 | 0.20 |
| 12(a) | $I$(CO) | $\sigma_{\rm rms} = 0.4$ K, $(t, e) = (5, 1.2)$ | 15.4 K km s$^{-1}$ | 0.50 | 0.18 |
| 12(a) | $I$(CO) | $\sigma_{\rm rms} = 0.6$ K, $(t, e) = (5, 1.2)$ | 21.0 K km s$^{-1}$ | 0.44 | 0.09 |
| 12(a) | $I$(CO) | $\sigma_{\rm rms} = 1.0$ K, $(t, e) = (5, 1.2)$ | 22.1 K km s$^{-1}$ | 0.43 | 0.14 |
| 12(a) | $I$(CO) | $\sigma_{\rm rms} = 2.0$ K, $(t, e) = (5, 1.2)$ | 62.0 K km s$^{-1}$ | 0.31 | 0.14 |
| 12(c) | $I$(CO) | $\sigma_{\rm rms} = 0.4$ K, $(t, e) = (3.5, 2)$ | 10.1 K km s$^{-1}$ | 0.66 | 0.13 |
| 12(c) | $I$(CO) | $\sigma_{\rm rms} = 0.6$ K, $(t, e) = (3.5, 2)$ | 21.1 K km s$^{-1}$ | 0.39 | 0.12 |
| 12(c) | $I$(CO) | $\sigma_{\rm rms} = 1.0$ K, $(t, e) = (3.5, 2)$ | 28.9 K km s$^{-1}$ | 0.33 | 0.11 |

**Notes.** Parameters of best-fitting functions to PDFs in Figure 9. The parameters of the LN functions are determined from a Levenberg–Marquardt fit to Equation (3). We use the logarithmic dispersion of the fit residuals to estimate the goodness of fit.

regions. Unlike the other methods, which tend to peak around $I$(CO) $\sim$ 20 km s$^{-1}$, the sigma-clipping method (M1) peaks at our nominal $3\sigma_{\rm rms}$ sensitivity limit. Even though we define $\sigma_{\rm rms}$ locally, i.e., we estimate $\sigma_{\rm rms}$ for each line of sight, inspection of the $I$(CO) map constructed using M1 reveals that many of these pixels come from the edge of the field where the brightness sensitivity of PAWS declines. Although this masking method is relatively common, we regard the resulting PDF to be the least reliable measure of the $I$(CO) distribution in M51's inner disk. In summary, while the different methods for constructing the $I$(CO) map yield PDFs that are different in detail, all the $I$(CO) PDFs except that obtained using M1 are roughly consistent with an LN function with mean $s_0 \sim 20$ K km s$^{-1}$ and logarithmic width $x = 0.4$, which we have indicated by a thick cyan line in Figure 9(a) (see also Table 3). Future studies should keep in mind that estimates for the shape of the $I$(CO) PDF are more likely to be dominated by systematic uncertainties due to different techniques for identifying significant emission than by simple counting and/or measurement errors.

As well as the $I$(CO) PDF, we tested the effect of different masking techniques on the shape of the $T_{\rm mb}$ PDF. The results for the central $140'' \times 90''$ of the PAWS field are presented in Figure 9(b); we do not construct PDFs using the entire field since the noise increases significantly toward the edge of the map (see Figure 1), which makes the resulting PDFs harder to interpret. For completeness, we also show the $T_{\rm mb}$ PDF of the PAWS cube without applying any mask (M0, gray histogram). Even though the total CO flux of the different masked and unmasked cubes agrees to within $\sim$30% (see Table 8 of Pety et al. 2013), the gray and magenta histograms (M0 and M1) only converge with the other PDFs for $T_{\rm mb} \gtrsim 2$ K. Below 2 K, the M0 and M1 histograms begin to curve upward, departing from the roughly LN shape of the distribution at higher intensities. The remaining PDFs are more similar, suggesting that the masking techniques that use additional criteria (e.g., proximity to a bright peak) are successful at retaining genuine emission at $\sim 3\sigma_{\rm rms}$, whereas a simple $3\sigma$ clip (i.e., masking method M1) may retain a significant number of isolated noise peaks. Nevertheless, some genuine low-brightness emission could be masked by methods M2–M5, although its spatial distribution is difficult to determine. In our analysis (Sections 4.1–4.4), we focus on the shape of the $I$(CO) and $T_{\rm mb}$ PDFs at relatively high brightness (i.e., brighter than $4\sigma_{\rm rms}$), so our results and interpretation should not be affected by the presence of such a faint emission component.

As for the $I$(CO) PDF, the smooth-and-mask method (M3) recovers the least emission at intermediate $T_{\rm mb}$ values ($1 < T_{\rm mb} < 3$ K) because compact, high-brightness regions are diluted beneath our $5\sigma_{\rm rms}$ threshold in the smoothed cube. The dilated mask technique (M2) yields a PDF that appears more like a broken power law with a turnover at $\sim$3 K. This variation is reasonable, since M2 should exclude some isolated regions of genuine emission that fall beneath our $5\sigma_{\rm rms}$ threshold, but include some noise at the edges of the mask with $T_{\rm mb} \sim 2\sigma_{\rm rms}$. For values above $\sim 3\sigma_{\rm rms}$, the $T_{\rm mb}$ PDFs for M2, M4, and M5 are practically identical, exhibiting a mean $T_{\rm mb} \sim 1.3$ K and logarithmic width $x \sim 0.35$.

We use our tailored mask, M5, for our analysis of the CO emission in the PAWS field (Section 4.1) and within different M51 environments (Section 4.3). As it closely reproduces the M5 results for M51, but is much simpler to implement across multiple data sets, we use the dilated mask technique (M2) for our comparative analysis of M51, the LMC, and M33 (Section 4.4).

## APPENDIX B
## RESOLUTION AND SENSITIVITY EFFECTS

Previous studies of the column density PDF for individual molecular clouds have shown that the shape of the PDF depends on the spatial resolution of the data (e.g., Froebrich & Rowles 2010). To assess the importance of this effect, we smoothed the original M51 data cube to angular resolutions of $1\farcs5$, $3''$, $6''$, $12''$, and $24''$, corresponding to linear scales of 60, 110, 230, 450, and 910 pc, respectively, for our assumed distance to M51. We constructed $I$(CO) maps from all the cubes after applying the dilated mask method to identify significant emission. The resulting $I$(CO) PDFs are presented in Figure 10(a), while the PDFs of CO brightness are shown in Figure 10(b). For the $I$(CO) PDFs, moderate variations in the resolution (i.e., up to $\sim$200 pc)

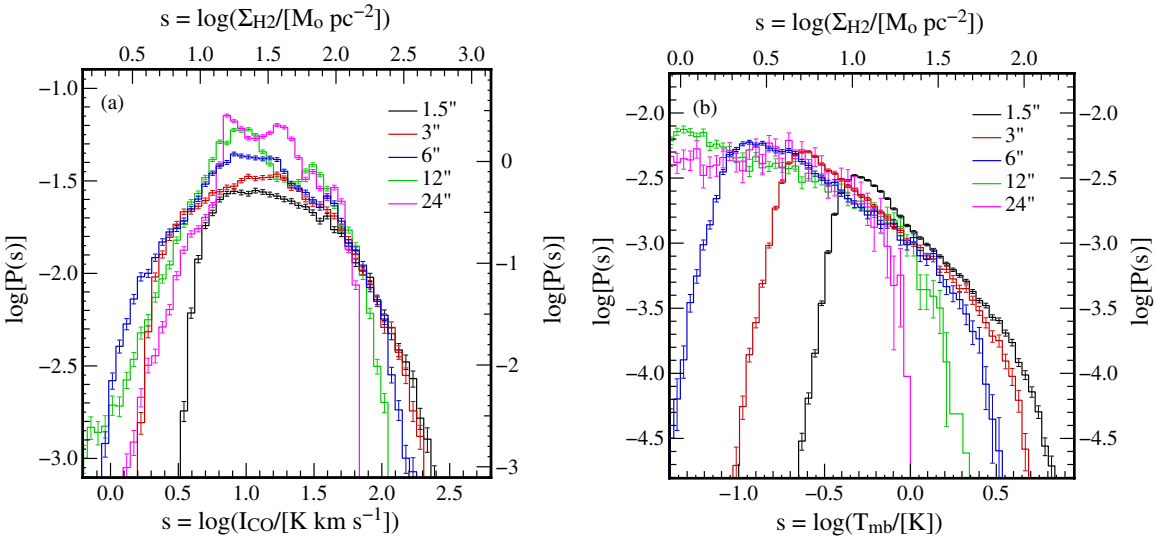


**Figure 10.** PDFs of (a) $I$(CO) and (b) $T_{\rm mb}$ within the PAWS field, obtained after convolving the original PAWS data cube with Gaussian smoothing kernels of varying width (see the text). The PDFs are obtained from cubes where significant emission is identified using a dilated mask method. The error bars represent the uncertainty associated with simple counting ($\sqrt{N}$) errors.

produce PDFs with a similar shape over a restricted range of $I$(CO) values (20–100 K km s$^{-1}$). It is striking, however, that the shape of the PDF at high intensities steepens as the angular resolution of the data cube is degraded. At ∼1 kpc resolution, the $I$(CO) PDF appears to show a threshold at $I$(CO) ∼ 60 K km s$^{-1}$; smoothing the data over even larger scales has no further effect. One kpc corresponds roughly to the radius of the central region and also to half the distance between the spiral arms. The appearance of an upper threshold would therefore seem to occur because the emission from these high-brightness regions is averaged together once the resolution is coarser than this spatial scale.

We obtain similar, although not identical, results for the $T_{\rm mb}$ PDFs. The slope of the PDFs at intermediate intensities (i.e., from $\sim 5\sigma_{\rm rms}$ to the $T_{\rm mb}$ value where the PDF begins to steepen) appears relatively constant, flattening slightly as the resolution degrades from a slope of $\sim -1.4$ at 60 pc resolution, to $\sim -0.7$ at 450 pc resolution. We note that this is the opposite trend to what is observed for the $I$(CO) PDFs, which become steeper at lower resolution. Like the $I$(CO) PDFs, however, the $T_{\rm mb}$ PDFs show a truncation that shifts to lower CO intensities as the smoothing scale increases. By ∼1 kpc resolution, the PDF has a sharp cut-off at $T_{\rm mb}$ ∼ 1 K for the same reason that the $I$(CO) PDF shows a threshold at this scale. The results of our resolution tests suggest that the appearance of thresholds and/or truncations in PDFs of gas emission tracers should therefore be interpreted with some caution, although these effects would appear to be most severe once the resolution of a data set becomes comparable to the characteristic spacing between regions of high brightness (i.e., the spacing between spiral arms and/or between SF complexes). Since the PAWS observations resolve these spatial scales, we do not regard resolution effects to be the main driver of the deviations from lognormality that we observe for the CO PDFs in Figures 4 and 5. The fact that the CO PDFs of M51's interarm regions do not show truncations at high intensities would further tend to support our interpretation that the truncations observed for the PDFs of the spiral arm and central environments are not solely due to limited spatial resolution. Since Galactic GMCs exhibit variations in their CO surface brightness, we would expect observations that spatially resolve internal structure of extragalactic clouds to reveal more features in the shape of the $I$(CO) and $T_{\rm mb}$ PDFs at high CO intensities (such as power-law tails due to the formation of strongly self-gravitating clumps; see, e.g., Kainulainen et al. 2009). While resolution effects do not seem to be the primary explanation for the variation in PDF shapes with galactic environment that we describe in Section 4, we therefore echo the recommendation by Wada & Norman (2007; see their Figure 7) that well-matched resolution is critical for comparative studies between observational data sets or between models and observations.

In addition to the effect of spatial resolution, we checked whether variations in the width of the velocity channels, i.e., the cube's spectral resolution, produced systematic changes in the shape of the $I$(CO) and $T_{\rm mb}$ PDFs. We constructed PDFs from cubes that had been folded along the velocity axis to 10, 20, 30, and 50 km s$^{-1}$and show the results in Figure 11. As the width of a velocity element increases, the $I$(CO) PDF narrows but the shape of distribution at high intensities ($I$(CO) $\gtrsim$ 50 K km s$^{-1}$) remains unchanged. The $T_{\rm mb}$ PDF broadens with increasing channel width, but its shape is also relatively robust. The maximum observed CO brightness declines by ∼3 K as the channel width increases from 5 to 50 km s$^{-1}$; this is due to the spectral equivalent of beam dilution.

In principle, the shape of the $I$(CO) and $T_{\rm mb}$ PDFs at high intensities should be relatively robust to noise, provided that the signal-to-noise ratio is sufficiently high. In practice, however, the sensitivity of most extragalactic $^{12}$CO($J = 1 \rightarrow 0$) mapping surveys is limited. In Figures 12(a) and (b), we show the PDFs of integrated intensity and CO brightness after adding increasing levels of Gaussian noise at the beam scale and using a dilated mask with $(t, e) = (5, 1.2)$ to identify regions of significant emission. For a moderate decrease in sensitivity ($\sigma_{\rm rms} \in [0.4, 1.0]$ K), the $I$(CO) PDFs retain their shape at high intensities (i.e., above ∼50 K km s$^{-1}$). Once the noise level is increased to $\sigma_{\rm rms} = 2$ K, however, the PDF begins to diverge significantly from the distribution obtained for the original cube, even at high intensities. This is because several regions in the nuclear bar and molecular ring regions are excluded from the mask once this noise level is added to the cube. High $I$(CO)

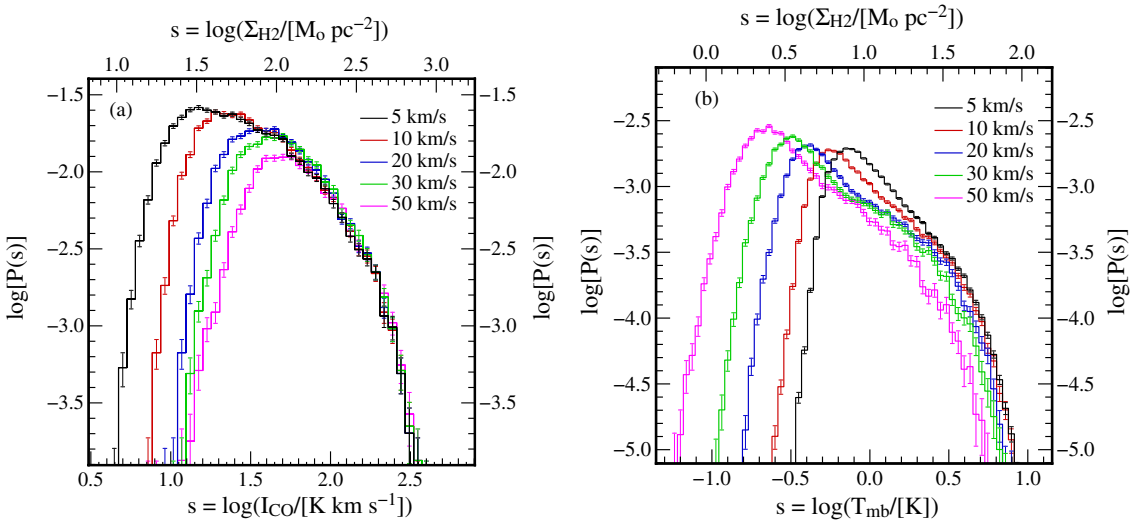


**Figure 11.** PDFs of (a) $I$(CO) and (b) $T_{\rm mb}$ within the PAWS field, obtained after folding the original PAWS data cube along the spectral axis to have velocity channels of varying width. The PDFs are obtained from the resulting cubes after identifying significant emission using a dilated mask method. The error bars represent the uncertainty associated with simple counting ($\sqrt{N}$) errors.

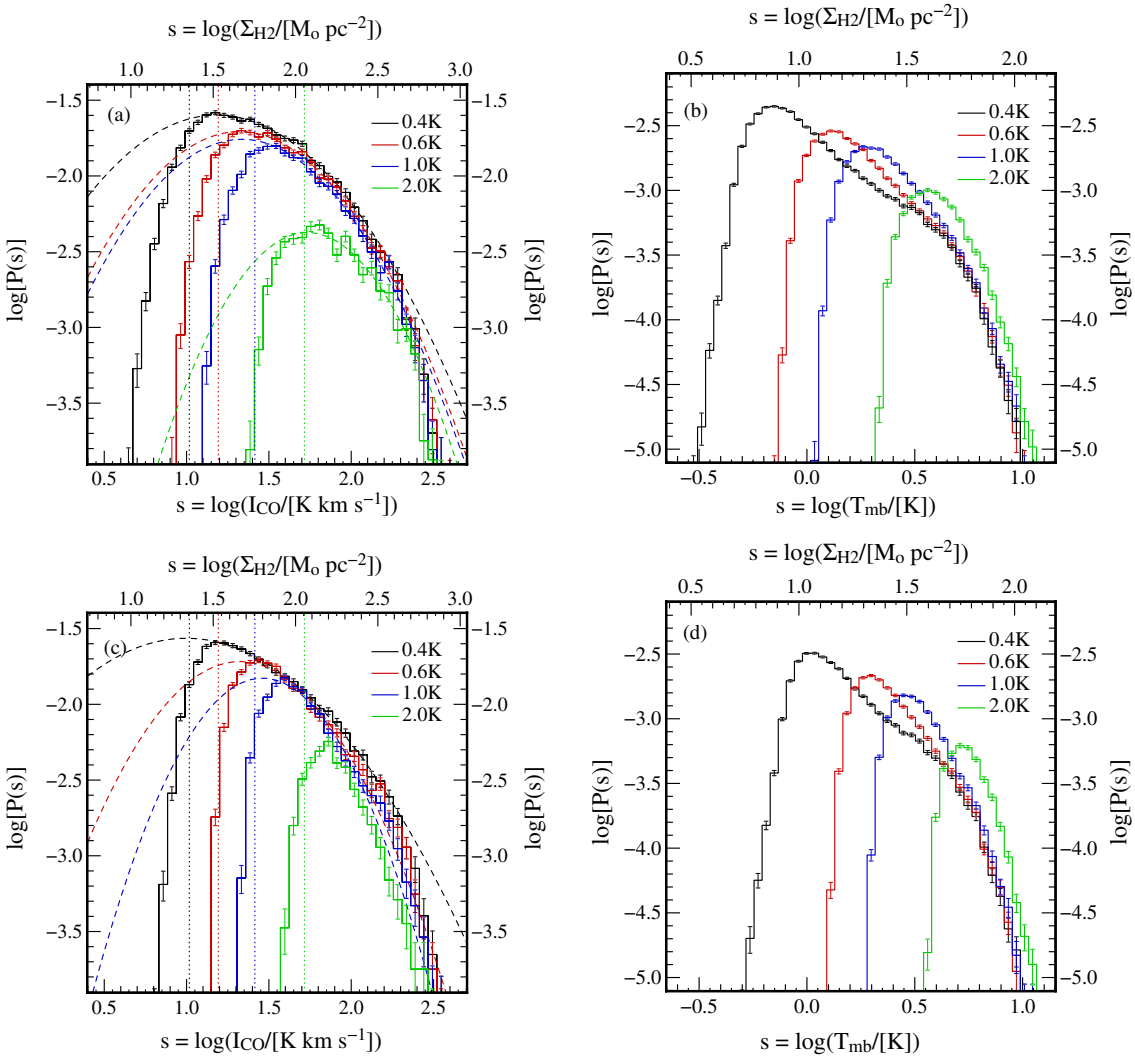


**Figure 12.** PDFs of $^{12}$CO($J = 1 \rightarrow 0$) integrated intensity (panels (a) and (c)) and CO brightness (panels (b) and (d)) within the PAWS field, obtained after adding Gaussian noise to the data cube at the beam scale. The PDFs were obtained from cubes where significant emission was identified using the dilated mask method with $(t, e) = (5, 1.2)$ (panels (a) and (b)) and $(t, e) = (3.5, 2)$ (panels (c) and (d)). In panels (a) and (c), the dashed parabola indicates the LN function that provides the best fit to the corresponding PDF. The vertical dotted lines indicate our nominal $3\sigma_{\rm rms}$ sensitivity limits. The PDFs in the panels (b) and (d) were obtained using the central quarter of the PAWS field only, to suppress effects that are caused by the lower signal-to-noise at the edge of the PAWS field. The error bars represent the uncertainty associated with simple counting ($\sqrt{N}$) errors.

measurements in these regions are often due to line profiles that are unusually wide (FWHM greater than $\sim$30 km s$^{-1}$) but have moderate brightness in individual channels, so they do not possess a bright core that lies above $5\sigma_{\rm rms} = 10$ K. Even for moderate levels of added noise ($\sigma_{\rm rms} \leqslant 1$ K), however, the best-fitting LN functions to the $I$(CO) PDFs in Figures 12(a) and (c) appear to narrow as the sensitivity decreases (see Table 3). This occurs even though we restrict the range of CO intensities used to estimate the fit to pixels where the emission is brighter than $4\sigma_{\rm rms}$. The dependence of the $I$(CO) PDF width on brightness sensitivity should be kept in mind when comparing the M51 PDFs with results from other galaxies or numerical simulations.

The $T_{\rm mb}$ PDFs from cubes with differing noise levels show more variation. Not surprisingly, the PDFs become narrower as the noise increases (since less emission satisfies our criteria for significance) but they also become steeper at low CO intensities, losing the appearance of a truncation at $T_{\rm mb} \sim 5$ K that is observed for the original cube. Since the construction of the dilated mask depends on the signal-to-noise, we examined whether similar trends were observed when we used different $(t, e)$ combinations to identify significant emission. As an example, $I$(CO) and $T_{\rm mb}$ PDFs for varying levels of noise using a dilated mask with $(t, e) = (3.5, 2)$ are shown in Figures 12(c) and (d), respectively. While these PDFs are not identical to the PDFs in panels (a) and (b), the effects of increasing the noise on the shape of PDFs that we have described are not sensitive to the particular combination of $(t, e)$ that we adopt to mask the input cubes.

## APPENDIX C

## ESTIMATING THE SLOPE OF THE GMC AND YOUNG CLUSTER MASS FUNCTIONS

For both GMCs and stellar clusters, the shape of the mass distribution is an important empirical signature of the physical processes that regulate their formation and disruption. The mass distribution is defined as the number of objects per unit mass, $f(M) = dN/dM$, and numerous studies have found that the mass distribution can be well described by a power law, $f(M) \propto M^{\beta}$, with a typical exponent of $\beta \approx -1.7$ (e.g., Rosolowsky 2005; Fukui & Kawamura 2010) for extragalactic GMCs identified in $^{12}$CO($J = 1 \rightarrow 0$) surveys and $\beta \approx -2.0$ for young star clusters (e.g., Chandar et al. 2010). An accurate determination of the shape of the mass distribution is crucial if it is to be used as a metric to quantify differences between and/or among populations of GMCs and clusters and hence to argue for (or against) the universality of the processes that determine their evolution. As noted by several authors, however, it can be difficult to measure the shape of the mass distribution robustly, especially when the sample of observed objects is small. Well-recognized sources of uncertainty include the method used to identify structures of interest (which usually depends on both resolution and sensitivity), the unambiguous determination of the low-mass completeness limit, inadequate sampling of the high-mass end of the distribution, uncertainty in mass measurements of individual objects, and (for mass distributions that model a differential formulation with a histogram) the choice of binning parameters. An added complication is that there are several "standard" methods for representing mass distributions employed by the GMC and stellar cluster research communities. In broad terms, studies of stellar cluster populations tend to adopt a differential formulation of the mass distribution, either separating the cluster mass measurements into bins of variable width with equal numbers of clusters in each bin or into bins of uniform logarithmic width but with a variable number of clusters in each bin, while it has become increasingly common for studies of GMC populations to represent the GMC mass distribution in cumulative form.

In light of these uncertainties and variations in technique, it is evident that any literature comparison between the parameters of mass distributions must be made with caution. In this Appendix, we estimate the uncertainty in the slope of the GMC and stellar cluster mass functions for different M51 environments by constructing the distributions using three common methods and by using different mass ranges in the linear regression that we use to fit the mass distribution. Our analysis falls short of being a general study of bias in mass distributions in at least two important ways. First, we model all the mass distributions as pure power laws and do not investigate other functional forms (such as a truncated power law or a Schechter function) that have been used to describe GMC and cluster populations. Second, we only examine a simple estimator—i.e., ordinary least squares linear regression—to determine the best-fitting power law to the mass functions. Since our main goal is to assess whether the trends discussed in Section 5.3 are robust, we consider it sufficient that we have used the same power-law model and statistical estimator for all the GMC and cluster mass distributions in our analysis. We refer the reader to other studies (e.g., Rosolowsky 2005; Reid et al. 2010) for more comprehensive investigations of the general problem of estimating the true mass distribution of objects from observational data.

In Figures 13–16, we plot example mass distributions for the GMCs and young (<10 Myr) clusters in the eight M51 environments that we examine in this paper. The distributions in Figures 13 and 15 are constructed using a cumulative representation, while those in Figures 14 and 16 are differential mass distributions for the same GMC/cluster populations, constructed using one example set of binning parameters. In each panel of Figures 14 and 16, we show both common forms of the differential mass distribution, i.e., a histogram with bins of equal logarithmic width (gray lines) and a histogram with equal number of objects per bin (black points). The black vertical dashed lines indicate the limiting mass range over which we estimate the fit for each distribution; the limits of this range were chosen so that the fit was calculated over an appreciable range of objects masses but avoiding regions of the mass distributions that show clear evidence for incompleteness effects (i.e., flattening) at low masses or truncation and/or sampling effects at high masses. The gray dot–dashed lines indicate the actual mass range that was used to obtain the fit in the examples shown.

The binning parameters and mass limits that were used in the linear regression for our trial fits to the mass distributions are listed in Table 4. For most environments, we tested mass ranges with lower (upper) limits $\log M_{\rm min,gmc} \in [5.8, 6.1]$ ($\log M_{\rm max,gmc} \in [6.5, 6.8]$) for GMCs and $\log M_{\rm min,cl} \in [3.6, 3.9]$ ($\log M_{\rm max,cl} \in [4.2, 4.4]$) for young clusters. Additionally, for the stellar clusters, we required that the mass range used to estimate the fit was larger than 0.4 dex, i.e., $\log M_{\rm max} > \log M_{\rm min} + 0.4$. For the fits to the differential mass spectra, bins containing fewer than two objects were excluded from the fit and the fit was only estimated when three or more

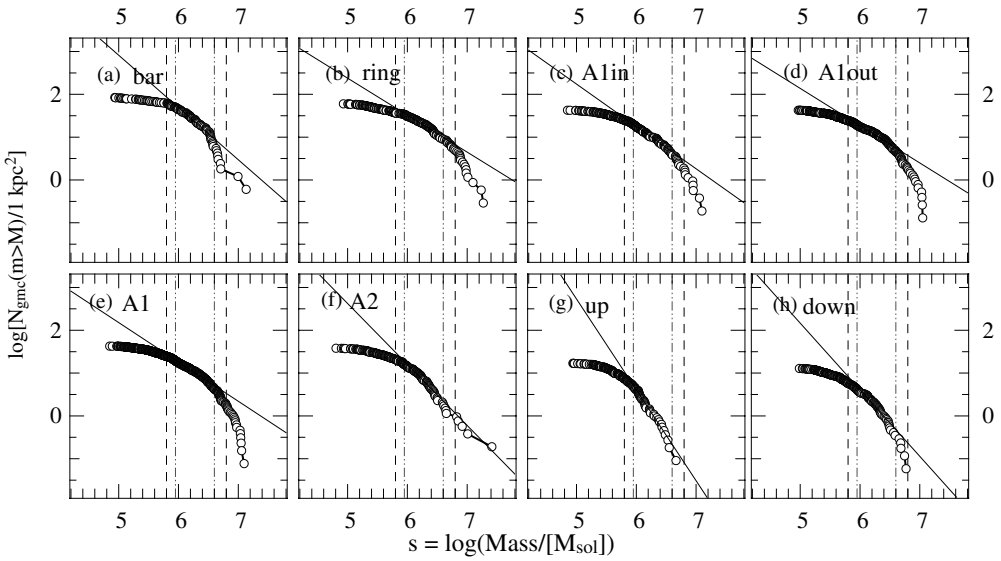


**Figure 13.** Cumulative mass distributions for GMCs in the different M51 environments. In each panel, the vertical dot–dashed lines indicate the mass range that was used to obtain the fit in the example shown. The black dashed lines indicate the limiting mass range over which we conduct the trials.

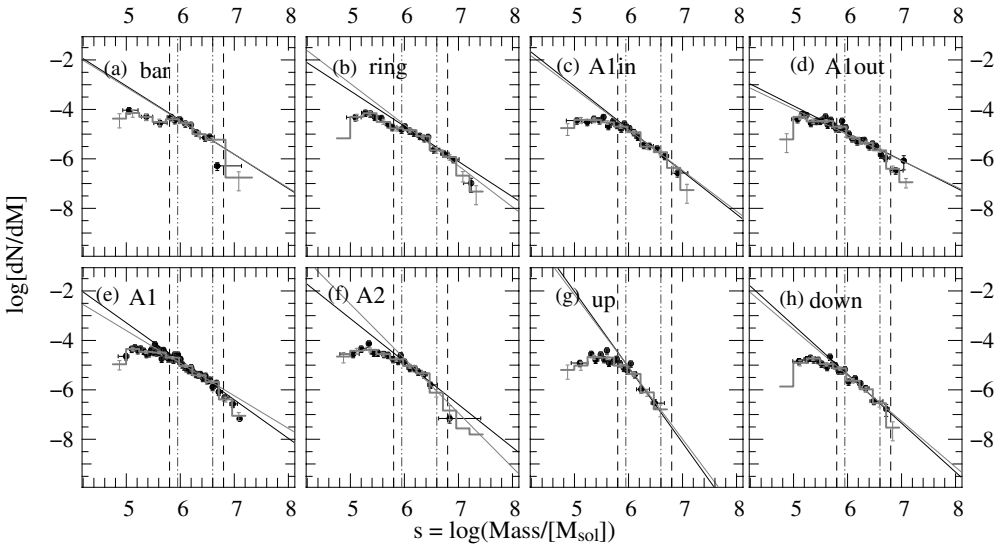


**Figure 14.** Differential mass distributions for GMCs in the different M51 environments. In each panel, the gray lines indicate a histogram with bins of equal logarithmic width, while the black points represent a histogram with equal number of GMCs per bin. Other plot annotations are the same as in Figure 13.

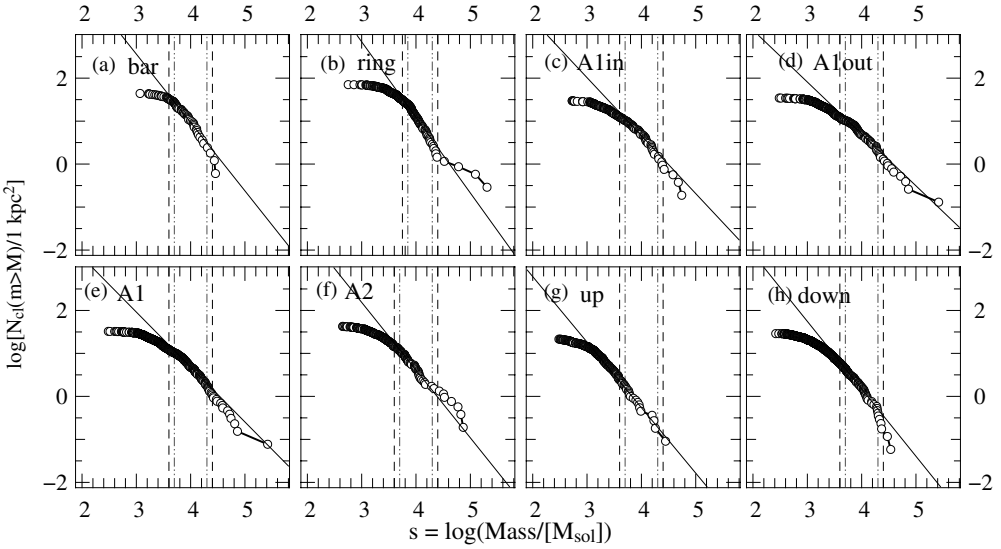


**Figure 15.** Cumulative mass distributions for young (<10 Myr) stellar clusters in the different M51 environments. Plot annotations are the same as in Figure 13.

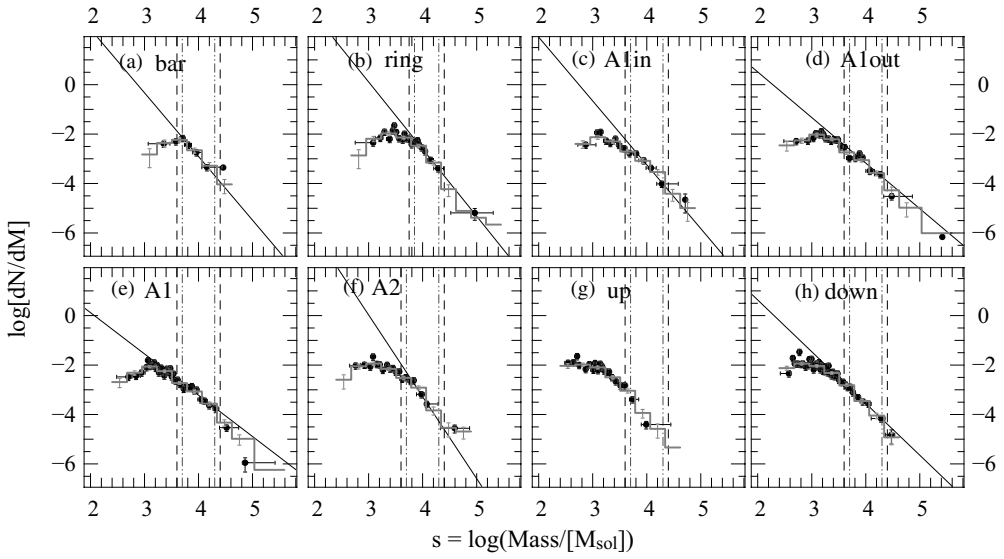


**Figure 16.** Differential mass distributions for young stellar clusters in the different M51 environments. Plot annotations are the same as in Figure 14.

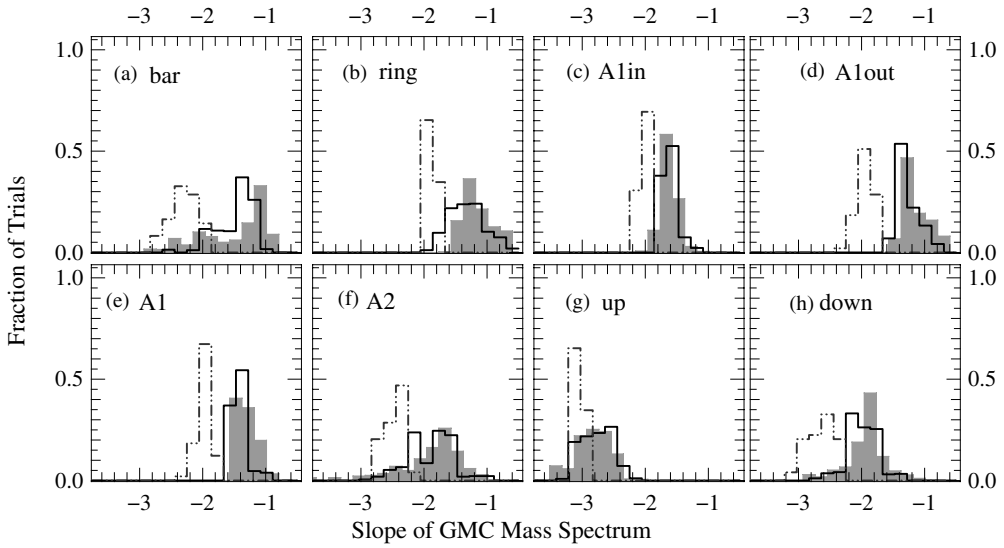


**Figure 17.** Histograms showing the distribution of slopes that we obtain from the trial fits to the cumulative (dot–dashed lines) and differential mass distributions of GMCs in different M51 environments. The black histograms indicate the slopes obtained from distributions constructed using bins of equal logarithmic width. The filled gray histograms represent the distribution of slopes for a mass function constructed using an equal number of GMCs per bin.

**Table 4**
Parameter Space Explored By GMC/Cluster Mass Distribution Trials

| Parameter | Range | Comment |
|---|---|---|
| $n_{\rm bin}$ | [8, 9, 10, 11, 12, 13, 14, 15, 16, 17, 18] | Number of histogram bins |
| $n_{\rm obj}$ | [8, 9, 10, 11, 12, 13, 14, 15, 16, 17, 18] | Number of GMCs/clusters in each bin |
| $\log M_{\rm min,cl}$[a] | [3.6, 3.65, 3.7, 3.75, 3.8, 3.85, 3.9] | Lower mass limit for fit to cluster mass distribution |
| $\log M_{\rm max,cl}$ | [4.2, 4.25, 4.3, 4.35, 4.4] | Upper mass limit for fit to cluster mass distribution |
| $\log M_{\rm min,gmc}$ | [5.8, 5.85, 5.9, 5.95, 6.0, 6.05, 6.10] | Lower mass limit for fit to GMC mass distribution |
| $\log M_{\rm max,gmc}$ | [6.5, 6.55, 6.6, 6.65, 6.7, 6.75, 6.8] | Upper mass limit for fit to GMC mass distribution |

**Note.** [a] Restricted to $\log M_{\rm min,cl} \in [3.75, 3.8, 3.85, 3.9]$ for fits to the cluster mass distribution in the ring region.

bins occupied the specified mass range. For the ring environment, the range of lower mass limits for stellar clusters was modified to $\log M_{\rm min,cl} \in [3.75, 3.9]$ because the mass distribution (see panel (b) of Figure 15) flattens sharply below $M \sim 6000\,M_\odot$. In principle, this flattening could have an observational origin (e.g., a higher completeness limit due to crowding/extinction in this region) or a physical origin (e.g., a higher probability of disruption for low-mass cluster objects). These possibilities will be explored in a future paper that investigates the shapes of the GMC and cluster mass distributions in detail; here, we simply reduce the mass range that we fit to the part of the distribution that conforms to a pure power law. In total, we obtained 35 (49) estimates of the cluster (GMC) mass distribution slope for each of the cumulative mass distributions and between 36 (362) and 385 (539) estimates for each of the differential mass distributions.

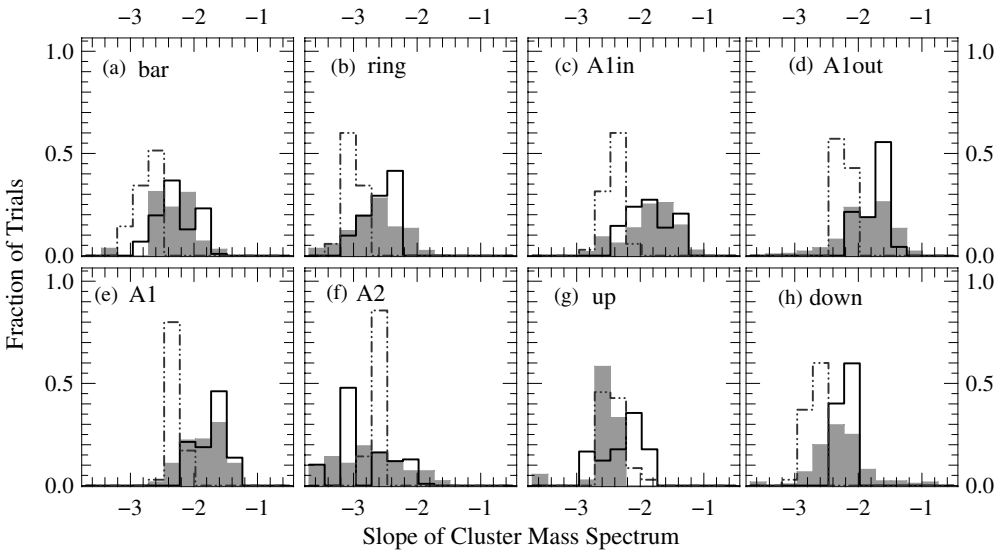


**Figure 18.** Same as Figure 17, but for young stellar clusters.

Histograms showing the distribution of slopes that we obtain from the trial fits are shown in Figures 17 and 18. For both GMCs and young clusters, it is evident that the slopes obtained using a cumulative representation of the mass distributions are systematically steeper (more negative) than for the differential formulation, although the offset between the peak of the histograms varies with environment. The discrepancy likely reflects the fact that the observed mass distributions are not pure power laws, but tend to steepen continuously across the observed range of masses. This steepening is not well captured by the differential distributions, since the values in each bin are weighted toward the lower-mass objects (which are more common) and hence a systematically shallower slope. The agreement between the two techniques is better for environments where the mass distribution more closely follows a pure power-law behavior (e.g., upstream of the spiral arms), consistent with this interpretation.

The slopes obtained for the differential mass distributions constructed using different binning strategies (i.e., the black and filled gray histograms in Figures 17 and 18) are generally in good agreement for the range of $n_{\rm obj}$ and $n_{\rm bin}$ values that we consider, but tend to show a larger dispersion than the fits obtained from the cumulative mass distributions. For some environments, the distribution of slopes is especially broad or shows evidence for bimodality. This is most evident for environments where there is a relatively sharp bend in the mass distribution within the mass range that we use to estimate the slopes, e.g., GMCs in the bar region (panel (a) of Figure 17) and clusters in the material arm (A2; panel (f) of Figure 18). Although we simply use the median of each environment for our analysis in Section 5.3 and capture the broader distribution in the uncertainties, it is worth noting that the relevant value of the slope in these environments may depend on the physical process under investigation and the range of masses over which that process is likely to be acting.

## REFERENCES


Aalto, S., Hüttemeister, S., Scoville, N. Z., & Thaddeus, P. 1999, ApJ, 522, 165
Alves, D. R. 2004, NewAR, 48, 659
Berkhuijsen, E. M., & Fletcher, A. 2008, MNRAS, 390, L19
Bigiel, F., Leroy, A., Walter, F., et al. 2008, AJ, 136, 2846
Bigiel, F., Leroy, A. K., Walter, F., et al. 2011, ApJL, 730, L13
Blitz, L. 1993, in Protostars and Planets III, ed. E. H. Levy & J. I. Lunine (Tucson, AZ: Univ. Arizona Press), 125
Block, D. L., Puerari, I., Elmegreen, B. G., & Bournaud, F. 2010, ApJL, 718, L1
Bournaud, F., Elmegreen, B. G., Teyssier, R., Block, D. L., & Puerari, I. 2010, MNRAS, 409, 1088
Brunt, C. M., Heyer, M. H., Vázquez-Semadeni, E., & Pichardo, B. 2003, ApJ, 595, 824
Chabrier, G., & Hennebelle, P. 2010, ApJL, 725, L79
Chandar, R., Whitmore, B. C., Calzetti, D., et al. 2011, ApJ, 727, 88
Chandar, R., Whitmore, B. C., Kim, H., et al. 2010, ApJ, 719, 966
Ciardullo, R., Feldmeier, J. J., Jacoby, G. H., et al. 2002, ApJ, 577, 31
Colombo, D., Meidt, S. E., Schinnerer, E., et al. 2013b, ApJ, submitted
Colombo, D., Schinnerer, E., Hughes, A., et al. 2013a, ApJ, submitted
Dame, T. M. 2011, arXiv:1101.1499
Dickman, R. L., Snell, R. L., & Schloerb, F. P. 1986, ApJ, 309, 326
Dobbs, C. L., Burkert, A., & Pringle, J. E. 2011, MNRAS, 417, 1318
Dobbs, C. L., Glover, S. C. O., Clark, P. C., & Klessen, R. S. 2008, MNRAS, 389, 1097
Dobbs, C. L., Theis, C., Pringle, J. E., & Bate, M. R. 2010, MNRAS, 403, 625
Egusa, F., Koda, J., & Scoville, N. 2011, ApJ, 726, 85
Elmegreen, B. G. 2002, ApJ, 577, 206
Elmegreen, B. G. 2011, ApJ, 731, 61
Elmegreen, B. G., & Falgarone, E. 1996, ApJ, 471, 816
Engargiola, G., Plambeck, R. L., Rosolowsky, E., & Blitz, L. 2003, ApJS, 149, 343
Fall, S. M., Krumholz, M. R., & Matzner, C. D. 2010, ApJL, 710, L142
Federrath, C., Klessen, R. S., & Schmidt, W. 2008, ApJL, 688, L79
Federrath, C., Roman-Duval, J., Klessen, R. S., Schmidt, W., & Mac Low, M.-M. 2010, A&A, 512, A81
Feldmann, R., Gnedin, N. Y., & Kravtsov, A. V. 2012, ApJ, 747, 124
Froebrich, D., & Rowles, J. 2010, MNRAS, 406, 1350
Fukui, Y., & Kawamura, A. 2010, ARA&A, 48, 547
Fukui, Y., Kawamura, A., Minamidani, T., et al. 2008, ApJS, 178, 56
Galleti, S., Bellazzini, M., & Ferraro, F. R. 2004, A&A, 423, 925
Garcia-Burillo, S., Guelin, M., & Cernicharo, J. 1993, A&A, 274, 123
Gaustad, J. E., & van Buren, D. 1993, PASP, 105, 1127
Georgelin, Y. M., & Georgelin, Y. P. 1976, A&A, 49, 57
Goldsmith, P. F., Heyer, M., Narayanan, G., et al. 2008, ApJ, 680, 428
Helfer, T. T., Thornley, M. D., Regan, M. W., et al. 2003, ApJS, 145, 259
Heyer, M., Krawczyk, C., Duval, J., & Jackson, J. M. 2009, ApJ, 699, 1092
Heyer, M. H., Corbelli, E., Schneider, S. E., & Young, J. S. 2004, ApJ, 602, 723
Hitschfeld, M., Kramer, C., Schuster, K. F., Garcia-Burillo, S., & Stutzki, J. 2009, A&A, 495, 795
Hopkins, P. F. 2012, MNRAS, 423, 2037
Hopkins, P. F., Quataert, E., & Murray, N. 2012, MNRAS, 421, 3488
Hughes, A., Meidt, S. E., Colombo, D., et al. 2013, ApJ, in press (arXiv:1309/3453)
Kainulainen, J., Beuther, H., Henning, T., & Plume, R. 2009, A&A, 508, L35
Kennicutt, R. C., Jr. 1998, ApJ, 498, 541
Koda, J., Scoville, N., Hasegawa, T., et al. 2012, ApJ, 761, 41
Koda, J., Scoville, N., Sawada, T., et al. 2009, ApJL, 700, L132

Kravtsov, A. V. 2003, ApJL, 590, L1
Krumholz, M. R., Dekel, A., & McKee, C. F. 2012, ApJ, 745, 69
Krumholz, M. R., & McKee, C. F. 2005, ApJ, 630, 250
Kuno, N., & Nakai, N. 1997, PASJ, 49, 279
Larson, R. B. 1981, MNRAS, 194, 809
Leroy, A. K., Bigiel, F., de Blok, W. J. G., et al. 2012, AJ, 144, 3
Liszt, H. S., Pety, J., & Lucas, R. 2010, A&A, 518, A45
Lombardi, M., Alves, J., & Lada, C. J. 2006, A&A, 454, 781
MacLaren, I., Richardson, K. M., & Wolfendale, A. W. 1988, ApJ, 333, 821
Meidt, S. E., Rand, R. J., Merrifield, M. R., Shetty, R., & Vogel, S. N. 2008, ApJ, 688, 224
Meidt, S. E., Schinnerer, E., García-Burillo, S., et al. 2013, ApJ, in press (arXiv:1304:7910)
Meidt, S. E., Schinnerer, E., Knapen, J. H., et al. 2012, ApJ, 744, 17
Mentuch Cooper, E., Wilson, C. D., Foyle, K., et al. 2012, ApJ, 755, 165
Mutchler, M., Beckwith, S. V. W., Bond, H., et al. 2005, BAAS, 37, 452
Padoan, P., & Nordlund, Å. 2002, ApJ, 576, 870
Padoan, P., Nordlund, A., & Jones, B. J. T. 1997, MNRAS, 288, 145
Pety, J. 2005, in SF2A-2005: Semaine de l'Astrophysique Francaise, ed. F. Casoli, T. Contini, J. M. Hameury, & L. Pagani (Paris: EdPSciences), 721
Pety, J., Schinnerer, E., Hughes, A., et al. 2013, ApJ, in press (arXiv:1304:1396)
Pineda, J. L., Mizuno, N., Stutzki, J., et al. 2008, A&A, 482, 197
Price, D. J., Federrath, C., & Brunt, C. M. 2011, ApJL, 727, L21
Rand, R. J. 1993, ApJ, 404, 593
Reid, M. A., Wadsley, J., Petitclerc, N., & Sills, A. 2010, ApJ, 719, 561
Rodriguez-Fernandez, N., Pety, J., & Gueth, F. 2008, Single-dish Observation and Processing to Produce the Short-spacing Information for a Millimeter Interferometer, Technical Memo IRAM 2008-2
Roman-Duval, J., Jackson, J. M., Heyer, M., Rathborne, J., & Simon, R. 2010, ApJ, 723, 492
Rosolowsky, E. 2005, PASP, 117, 1403
Rosolowsky, E., Keto, E., Matsushita, S., & Willner, S. P. 2007, ApJ, 661, 830
Rosolowsky, E., & Leroy, A. 2006, PASP, 118, 590
Sanders, D. B., Scoville, N. Z., & Solomon, P. M. 1985, ApJ, 289, 373
Sawada, T., Hasegawa, T., & Koda, J. 2012a, ApJL, 759, L26
Sawada, T., Hasegawa, T., Sugimoto, M., Koda, J., & Handa, T. 2012b, ApJ, 752, 118
Schinnerer, E., Meidt, S. E., Colombo, D., et al. 2013, ApJ, in press (arXiv:1304.1801)
Schinnerer, E., Weiß, A., Aalto, S., & Scoville, N. Z. 2010, ApJ, 719, 1588
Schmidt, M. 1959, ApJ, 129, 243
Schuster, K. F., Kramer, C., Hitschfeld, M., Garcia-Burillo, S., & Mookerjea, B. 2007, A&A, 461, 143
Shetty, R., Glover, S. C., Dullemond, C. P., & Klessen, R. S. 2011, MNRAS, 412, 1686
Shetty, R., Vogel, S. N., Ostriker, E. C., & Teuben, P. J. 2007, ApJ, 665, 1138
Solomon, P. M., Rivolo, A. R., Barrett, J., & Yahil, A. 1987, ApJ, 319, 730
Tan, Q.-H., Gao, Y., Zhang, Z.-Y., & Xia, X.-Y. 2011, RAA, 11, 787
Tasker, E. J., & Bryan, G. L. 2006, ApJ, 641, 878
Tasker, E. J., & Tan, J. C. 2009, ApJ, 700, 358
Tosaki, T., Hasegawa, T., Shioya, Y., Kuno, N., & Matsushita, S. 2002, PASJ, 54, 209
Vazquez-Semadeni, E. 1994, ApJ, 423, 681
Vogel, S. N., Kulkarni, S. R., & Scoville, N. Z. 1988, Natur, 334, 402
Vogel, S. N., Rand, R. J., Gruendl, R. A., & Teuben, P. J. 1993, PASP, 105, 666
Wada, K., & Norman, C. A. 2001, ApJ, 547, 172
Wada, K., & Norman, C. A. 2007, ApJ, 660, 276
Wada, K., Spaans, M., & Kim, S. 2000, ApJ, 540, 797
Wolfire, M. G., Hollenbach, D., & McKee, C. F. 2010, ApJ, 716, 1191
Wong, T., & Blitz, L. 2002, ApJ, 569, 157
Wong, T., Hughes, A., Ott, J., et al. 2011, ApJS, 197, 16
Zaritsky, D., Rix, H.-W., & Rieke, M. 1993, Natur, 364, 313